EUROPEAN ORGANIZATION FOR NUCLEAR RESEARCH

ZZ production in e^+e^- interactions at $\sqrt{s} = 183 - 209$ GeV

DELPHI Collaboration

Abstract

Measurements of on-shell ZZ production are described, using data from the DELPHI experiment at LEP in e^+e^- collisions at centre-of-mass energies between 183 and 209 GeV, corresponding to an integrated luminosity of about 665 pb^{-1}. Results obtained in each of the final states $q\bar{q}q\bar{q}$, $\nu\bar{\nu}q\bar{q}$, $\mu^+\mu^-q\bar{q}$, $e^+e^-q\bar{q}$, $\tau^+\tau^-q\bar{q}$, $l^+l^-l^+l^-$, and $\nu\bar{\nu}l^+l^-$ (with $l = e, \mu$) are presented. The measured production cross-sections are consistent with the Standard Model expectations. These results update and supersede those already published at 183 and 189 GeV.

J.Abdallah[25], P.Abreu[22], W.Adam[51], P.Adzic[11], T.Albrecht[17], T.Alderweireld[2], R.Alemany-Fernandez[8], T.Allmendinger[17], P.P.Allport[23], U.Amaldi[29], N.Amapane[45], S.Amato[48], E.Anashkin[36], A.Andreazza[28], S.Andringa[22], N.Anjos[22], P.Antilogus[27], W-D.Apel[17], Y.Arnoud[14], S.Ask[26], B.Asman[44], J.E.Augustin[25], A.Augustinus[8], P.Baillon[8], A.Ballestrero[46], P.Bambade[20], R.Barbier[27], D.Bardin[16], G.Barker[17], A.Baroncelli[39], M.Battaglia[8], M.Baubillier[25], K-H.Becks[53], M.Begalli[6], A.Behrmann[53], E.Ben-Haim[20], N.Benekos[32], A.Benvenuti[5], C.Berat[14], M.Berggren[25], L.Berntzon[44], D.Bertrand[2], M.Besancon[40], N.Besson[40], D.Bloch[9], M.Blom[31], M.Bluj[52], M.Bonesini[29], M.Boonekamp[40], P.S.L.Booth[23], G.Borisov[21], O.Botner[49], B.Bouquet[20], T.J.V.Bowcock[23], I.Boyko[16], M.Bracko[43], R.Brenner[49], E.Brodet[35], P.Bruckman[18], J.M.Brunet[7], L.Bugge[33], P.Buschmann[53], M.Calvi[29], T.Camporesi[8], V.Canale[38], F.Carena[8], N.Castro[22], F.Cavallo[5], M.Chapkin[42], Ph.Charpentier[8], P.Checchia[36], R.Chierici[8], P.Chliapnikov[42], J.Chudoba[8], S.U.Chung[8], K.Cieslik[18], P.Collins[8], R.Contri[13], G.Cosme[20], F.Cossutti[47], M.J.Costa[50], B.Crawley[1], D.Crennell[37], J.Cuevas[34], J.D'Hondt[2], J.Dalmau[44], T.da Silva[48], W.Da Silva[25], G.Della Ricca[47], A.De Angelis[47], W.De Boer[17], C.De Clercq[2], B.De Lotto[47], N.De Maria[45], A.De Min[36], L.de Paula[48], L.Di Ciaccio[38], A.Di Simone[39], K.Doroba[52], J.Drees[53,8], M.Dris[32], G.Eigen[4], T.Ekelof[49], M.Ellert[49], M.Elsing[8], M.C.Espirito Santo[22], G.Fanourakis[11], D.Fassouliotis[11,3], M.Feindt[17], J.Fernandez[41], A.Ferrer[50], F.Ferro[13], U.Flagmeyer[53], H.Foeth[8], E.Fokitis[32], F.Fulda-Quenzer[20], J.Fuster[50], M.Gandelman[48], C.Garcia[50], Ph.Gavillet[8], E.Gazis[32], R.Gokieli[8,52], B.Golob[43], G.Gomez-Ceballos[41], P.Goncalves[22], E.Graziani[39], G.Grosdidier[20], K.Grzelak[52], J.Guy[37], C.Haag[17], A.Hallgren[49], K.Hamacher[53], K.Hamilton[35], J.Hansen[33], S.Haug[33], F.Hauler[17], V.Hedberg[26], M.Hennecke[17], H.Herr[8], J.Hoffman[52], S-O.Holmgren[44], P.J.Holt[8], M.A.Houlden[23], K.Hultqvist[44], J.N.Jackson[23], G.Jarlskog[26], P.Jarry[40], D.Jeans[35], E.K.Johansson[44], P.D.Johansson[44], P.Jonsson[27], C.Joram[8], L.Jungermann[17], F.Kapusta[25], S.Katsanevas[27], E.Katsoufis[32], G.Kernel[43], B.P.Kersevan[8,43], A.Kiiskinen[15], B.T.King[23], N.J.Kjaer[8], P.Kluit[31], P.Kokkinias[11], C.Kourkoumelis[3], O.Kouznetsov[16], Z.Krumstein[16], M.Kucharczyk[18], J.Lamsa[1], G.Leder[51], F.Ledroit[14], L.Leinonen[44], R.Leitner[30], J.Lemonne[2], V.Lepeltier[20], T.Lesiak[18], W.Liebig[53], D.Liko[51], A.Lipniacka[44], J.H.Lopes[48], J.M.Lopez[34], D.Loukas[11], P.Lutz[40], L.Lyons[35], J.MacNaughton[51], A.Malek[53], S.Maltezos[32], F.Mandl[51], J.Marco[41], R.Marco[41], B.Marechal[48], M.Margoni[36], J-C.Marin[8], C.Mariotti[8], A.Markou[11], C.Martinez-Rivero[41], J.Masik[12], N.Mastroyiannopoulos[11], F.Matorras[41], C.Matteuzzi[29], F.Mazzucato[36], M.Mazzucato[36], R.Mc Nulty[23], C.Meroni[28], W.T.Meyer[1], E.Migliore[45], W.Mitaroff[51], U.Mjoernmark[26], T.Moa[44], M.Moch[17], K.Moenig[8,10], R.Monge[13], J.Montenegro[31], D.Moraes[48], S.Moreno[22], P.Morettini[13], U.Mueller[53], K.Muenich[53], M.Mulders[31], L.Mundim[6], W.Murray[37], B.Muryn[19], G.Myatt[35], T.Myklebust[33], M.Nassiakou[11], F.Navarria[5], K.Nawrocki[52], R.Nicolaidou[40], M.Nikolenko[16,9], A.Oblakowska-Mucha[19], V.Obraztsov[42], A.Olshevski[16], A.Onofre[22], R.Orava[15], K.Osterberg[15], A.Ouraou[40], A.Oyanguren[50], M.Paganoni[29], S.Paiano[5], J.P.Palacios[23], H.Palka[18], Th.D.Papadopoulou[32], L.Pape[8], C.Parkes[24], F.Parodi[13], U.Parzefall[8], A.Passeri[39], O.Passon[53], L.Peralta[22], V.Perepelitsa[50], A.Perrotta[5], A.Petrolini[13], J.Piedra[41], L.Pieri[39], F.Pierre[40], M.Pimenta[22], E.Piotto[8], T.Podobnik[43], V.Poireau[8], M.E.Pol[6], G.Polok[18], P.Poropat[†47], V.Pozdniakov[16], N.Pukhaeva[2,16], A.Pullia[29], J.Rames[12], L.Ramler[17], A.Read[33], P.Rebecchi[8], J.Rehn[17], D.Reid[31], R.Reinhardt[53], P.Renton[35], F.Richard[20], J.Ridky[12], M.Rivero[41], D.Rodriguez[41], A.Romero[45], P.Ronchese[36], E.Rosenberg[1], P.Roudeau[20], T.Rovelli[5], V.Ruhlmann-Kleider[40], D.Ryabtchikov[42], A.Sadovsky[16], L.Salmi[15], J.Salt[50], A.Savoy-Navarro[25], U.Schwickerath[8], A.Segar[35], R.Sekulin[37], M.Siebel[53], A.Sisakian[16], G.Smadja[27], O.Smirnova[26], A.Sokolov[42], A.Sopczak[21], R.Sosnowski[52], T.Spassov[8], M.Stanitzki[17], A.Stocchi[20], J.Strauss[51], B.Stugu[4], M.Szczekowski[52], M.Szeptycka[52], T.Szumlak[19], T.Tabarelli[29], A.C.Taffard[23], F.Tegenfeldt[49], J.Timmermans[31], L.Tkatchev[16], M.Tobin[23], S.Todorovova[12], B.Tome[22], A.Tonazzo[29], P.Tortosa[50], P.Travnicek[12], D.Treille[8], G.Tristram[7], M.Trochimczuk[52], C.Troncon[28], M-L.Turluer[40], I.A.Tyapkin[16], P.Tyapkin[16], S.Tzamarias[11], V.Uvarov[42], G.Valenti[5], P.Van Dam[31], J.Van Eldik[8], A.Van Lysebetten[2], N.van Remortel[2], I.Van Vulpen[8], G.Vegni[28], F.Veloso[22], W.Venus[37], F.Verbeure[2], P.Verdier[27], V.Verzi[38], D.Vilanova[40], L.Vitale[47], V.Vrba[12], H.Wahlen[53], A.J.Washbrook[23], C.Weiser[17],

D.Wicke[8], J.Wickens[2], G.Wilkinson[35], M.Winter[9], M.Witek[18], O.Yushchenko[42], A.Zalewska[18], P.Zalewski[52], D.Zavrtanik[43], V.Zhuravlov[16], N.I.Zimin[16], A.Zintchenko[16], M.Zupan[11]

[1]Department of Physics and Astronomy, Iowa State University, Ames IA 50011-3160, USA
[2]Physics Department, Universiteit Antwerpen, Universiteitsplein 1, B-2610 Antwerpen, Belgium
  and IIHE, ULB-VUB, Pleinlaan 2, B-1050 Brussels, Belgium
  and Faculté des Sciences, Univ. de l'Etat Mons, Av. Maistriau 19, B-7000 Mons, Belgium
[3]Physics Laboratory, University of Athens, Solonos Str. 104, GR-10680 Athens, Greece
[4]Department of Physics, University of Bergen, Allégaten 55, NO-5007 Bergen, Norway
[5]Dipartimento di Fisica, Università di Bologna and INFN, Via Irnerio 46, IT-40126 Bologna, Italy
[6]Centro Brasileiro de Pesquisas Físicas, rua Xavier Sigaud 150, BR-22290 Rio de Janeiro, Brazil
  and Depto. de Física, Pont. Univ. Católica, C.P. 38071 BR-22453 Rio de Janeiro, Brazil
  and Inst. de Física, Univ. Estadual do Rio de Janeiro, rua São Francisco Xavier 524, Rio de Janeiro, Brazil
[7]Collège de France, Lab. de Physique Corpusculaire, IN2P3-CNRS, FR-75231 Paris Cedex 05, France
[8]CERN, CH-1211 Geneva 23, Switzerland
[9]Institut de Recherches Subatomiques, IN2P3 - CNRS/ULP - BP20, FR-67037 Strasbourg Cedex, France
[10]Now at DESY-Zeuthen, Platanenallee 6, D-15735 Zeuthen, Germany
[11]Institute of Nuclear Physics, N.C.S.R. Demokritos, P.O. Box 60228, GR-15310 Athens, Greece
[12]FZU, Inst. of Phys. of the C.A.S. High Energy Physics Division, Na Slovance 2, CZ-180 40, Praha 8, Czech Republic
[13]Dipartimento di Fisica, Università di Genova and INFN, Via Dodecaneso 33, IT-16146 Genova, Italy
[14]Institut des Sciences Nucléaires, IN2P3-CNRS, Université de Grenoble 1, FR-38026 Grenoble Cedex, France
[15]Helsinki Institute of Physics, P.O. Box 64, FIN-00014 University of Helsinki, Finland
[16]Joint Institute for Nuclear Research, Dubna, Head Post Office, P.O. Box 79, RU-101 000 Moscow, Russian Federation
[17]Institut für Experimentelle Kernphysik, Universität Karlsruhe, Postfach 6980, DE-76128 Karlsruhe, Germany
[18]Institute of Nuclear Physics,Ul. Kawiory 26a, PL-30055 Krakow, Poland
[19]Faculty of Physics and Nuclear Techniques, University of Mining and Metallurgy, PL-30055 Krakow, Poland
[20]Université de Paris-Sud, Lab. de l'Accélérateur Linéaire, IN2P3-CNRS, Bât. 200, FR-91405 Orsay Cedex, France
[21]School of Physics and Chemistry, University of Lancaster, Lancaster LA1 4YB, UK
[22]LIP, IST, FCUL - Av. Elias Garcia, 14-1°, PT-1000 Lisboa Codex, Portugal
[23]Department of Physics, University of Liverpool, P.O. Box 147, Liverpool L69 3BX, UK
[24]Dept. of Physics and Astronomy, Kelvin Building, University of Glasgow, Glasgow G12 8QQ
[25]LPNHE, IN2P3-CNRS, Univ. Paris VI et VII, Tour 33 (RdC), 4 place Jussieu, FR-75252 Paris Cedex 05, France
[26]Department of Physics, University of Lund, Sölvegatan 14, SE-223 63 Lund, Sweden
[27]Université Claude Bernard de Lyon, IPNL, IN2P3-CNRS, FR-69622 Villeurbanne Cedex, France
[28]Dipartimento di Fisica, Università di Milano and INFN-MILANO, Via Celoria 16, IT-20133 Milan, Italy
[29]Dipartimento di Fisica, Univ. di Milano-Bicocca and INFN-MILANO, Piazza della Scienza 2, IT-20126 Milan, Italy
[30]IPNP of MFF, Charles Univ., Areal MFF, V Holesovickach 2, CZ-180 00, Praha 8, Czech Republic
[31]NIKHEF, Postbus 41882, NL-1009 DB Amsterdam, The Netherlands
[32]National Technical University, Physics Department, Zografou Campus, GR-15773 Athens, Greece
[33]Physics Department, University of Oslo, Blindern, NO-0316 Oslo, Norway
[34]Dpto. Fisica, Univ. Oviedo, Avda. Calvo Sotelo s/n, ES-33007 Oviedo, Spain
[35]Department of Physics, University of Oxford, Keble Road, Oxford OX1 3RH, UK
[36]Dipartimento di Fisica, Università di Padova and INFN, Via Marzolo 8, IT-35131 Padua, Italy
[37]Rutherford Appleton Laboratory, Chilton, Didcot OX11 OQX, UK
[38]Dipartimento di Fisica, Università di Roma II and INFN, Tor Vergata, IT-00173 Rome, Italy
[39]Dipartimento di Fisica, Università di Roma III and INFN, Via della Vasca Navale 84, IT-00146 Rome, Italy
[40]DAPNIA/Service de Physique des Particules, CEA-Saclay, FR-91191 Gif-sur-Yvette Cedex, France
[41]Instituto de Fisica de Cantabria (CSIC-UC), Avda. los Castros s/n, ES-39006 Santander, Spain
[42]Inst. for High Energy Physics, Serpukov P.O. Box 35, Protvino, (Moscow Region), Russian Federation
[43]J. Stefan Institute, Jamova 39, SI-1000 Ljubljana, Slovenia and Laboratory for Astroparticle Physics,
  Nova Gorica Polytechnic, Kostanjeviska 16a, SI-5000 Nova Gorica, Slovenia,
  and Department of Physics, University of Ljubljana, SI-1000 Ljubljana, Slovenia
[44]Fysikum, Stockholm University, Box 6730, SE-113 85 Stockholm, Sweden
[45]Dipartimento di Fisica Sperimentale, Università di Torino and INFN, Via P. Giuria 1, IT-10125 Turin, Italy
[46]INFN,Sezione di Torino, and Dipartimento di Fisica Teorica, Università di Torino, Via P. Giuria 1,
  IT-10125 Turin, Italy
[47]Dipartimento di Fisica, Università di Trieste and INFN, Via A. Valerio 2, IT-34127 Trieste, Italy
  and Istituto di Fisica, Università di Udine, IT-33100 Udine, Italy
[48]Univ. Federal do Rio de Janeiro, C.P. 68528 Cidade Univ., Ilha do Fundão BR-21945-970 Rio de Janeiro, Brazil
[49]Department of Radiation Sciences, University of Uppsala, P.O. Box 535, SE-751 21 Uppsala, Sweden
[50]IFIC, Valencia-CSIC, and D.F.A.M.N., U. de Valencia, Avda. Dr. Moliner 50, ES-46100 Burjassot (Valencia), Spain
[51]Institut für Hochenergiephysik, Österr. Akad. d. Wissensch., Nikolsdorfergasse 18, AT-1050 Vienna, Austria
[52]Inst. Nuclear Studies and University of Warsaw, Ul. Hoza 69, PL-00681 Warsaw, Poland
[53]Fachbereich Physik, University of Wuppertal, Postfach 100 127, DE-42097 Wuppertal, Germany
† deceased

1   Introduction

The first evidence [1] for doubly resonant production of Z bosons was observed during 1997, when the LEP-2 accelerator reached a centre-of-mass energy near 183 GeV, corresponding to the threshold for this channel. In this article we present measurements of the production cross-section, using data collected by the DELPHI experiment in 1997-2000, at centre-of-mass energies up to 209 GeV, corresponding to an integrated luminosity of about 665 pb^{-1}.

There are several motivations for studying this channel. Firstly, it enables a check of the Standard Model (SM) prediction. Both the cross-section and angular distribution of the produced Z bosons are sensitive to contributions from new physics beyond the SM. Several mechanisms for anomalous production [2,3] can hence be constrained directly. For instance, limits on neutral triple gauge boson couplings [4], which are forbidden in the SM, can be set [5]. Secondly, the ZZ production process is an almost irreducible background to the Higgs search at LEP, particularly when the mass of the Higgs boson is close to that of the Z [6]. It provides an environment similar to that corresponding to a possible Higgs signal, in the main final state topologies which are analysed, both in terms of experimental signature and rate. In this context, it allows to test the techniques used in the Higgs analyses on an existing process.

In what follows, the data sets and simulations used are described and the signal definition adopted is discussed. The event selections are presented for each of the seven sub-channels which were analysed: $q\bar{q}q\bar{q}$, $\nu\bar{\nu}q\bar{q}$, $\mu^+\mu^-q\bar{q}$, $e^+e^-q\bar{q}$, $\tau^+\tau^-q\bar{q}$, $l^+l^-l^+l^-$, and $\nu\bar{\nu}l^+l^-$ (with $l = e, \mu$). Results are given in the form of a comparison of the numbers of observed and predicted selected events, together with an evaluation of the main systematic effects. Finally, combinations of sub-channel results into overall ZZ cross-sections at each centre-of-mass energy are described, as well as combinations performed over all centre-of-mass energies, both separately in each sub-channel, and for all channels together. The resulting measurements are compared with SM expectations.

These results update and supersede those already published at 183 and 189 GeV [7], by including the $\tau^+\tau^-q\bar{q}$ sub-channel and using improved methods in several of the other channels. Measurements of on-shell ZZ production published by the three other LEP collaborations can be found in [1,8–10].

2   Data samples and simulation

The data samples used were collected by DELPHI in the years 1997-2000. The corresponding centre-of-mass energies and integrated luminosities which were analysed are given in Table 1. A detailed description of the detector and a review of its performance can be found in [11,12]. For LEP-2 operation, the vertex detector was upgraded [13] and a set of scintillator counters was added to veto photons in blind regions of the electromagnetic calorimetry, at polar angles $\theta \simeq 40°$, $90°$ and $140°$.

Simulated events were produced with the DELPHI simulation program `DELSIM` [12] and were then passed through the same reconstruction and analysis chain as the data. The generation of processes leading to four-fermion final states was done with `EXCALIBUR` [14], relying on `JETSET` 7.4 [15] for quark fragmentation. `GRC4F` [16] was used as a complementary generator for four-fermion final states resulting from single-resonant $We\nu_e$ and $(Z/\gamma^*)e^+e^-$ processes when the spectator electron was close to the beam direction. Two-fermion processes $e^+e^- \rightarrow q\bar{q}(\gamma)$ were generated using `PYTHIA` [15], $e^+e^- \rightarrow \mu^+\mu^-(\gamma)$ and $e^+e^- \rightarrow \tau^+\tau^-(\gamma)$ with `KORALZ` [17], and $e^+e^- \rightarrow e^+e^-(\gamma)$ with `BHWIDE` [18]. Two-photon

interactions were generated using TWOGAM [19] and BDK [20]. The sizes of the simulated event samples were typically at least 100 times larger than expected in real data.

One sector (corresponding to 1/12) of the main tracking device, the Time Projection Chamber, was inactive for the last quarter of the 2000 data sample. The corresponding small change of analysis sensitivity from this period was studied with specially made simulations and taken into account in the extraction of the cross-sections.

Year	$\sqrt{s}$ [GeV]	Integrated luminosity [pb^{-1}]
1997	182.6	54.0
1998	188.6	158.1
1999	191.6	25.8
1999	195.5	76.9
1999	199.5	84.3
1999	201.6	41.1
2000	< 205.5	83.3
2000	> 205.5	141.8
Total	-	665.3

Table 1: Centre-of-mass energies and integrated luminosities of the analysed data. During the year 2000, the energies reached were in the range 202-209 GeV, clustered mainly around 205 and 207 GeV.

3 Signal definition in the simulation

Figure 1: The Feynman graphs for on-shell ZZ production (referred to as the NC02 graphs)

The region of phase-space at high di-fermion masses which characterizes ZZ production must be isolated to measure the corresponding cross-section. In this region, besides the dominant tree-level doubly-resonant ZZ production graphs shown in Figure 1 (referred to as the NC02 graphs), there are also contributions from other four-fermion processes, which can lead to identical final states[1]. In order to interpret the measurements in terms of NC02 graphs, the ZZ signal was defined in each of the sub-channels

---

[1]Such contributions arise from $e^+e^- \to (Z/\gamma^*)\gamma^*$ processes (when γ^* virtualities are close to the Z boson mass), from $(Z/\gamma^*)e^+e^-$ processes (in cases of final states with electrons), and from processes involving W bosons (in cases of $u\bar{u}d\bar{d}$, $c\bar{c}s\bar{s}$, and $\nu_l\bar{\nu}_l l^+l^-$ final states).

by pre-selecting a sub-set of events within the four-fermion simulation, having both a high purity and efficiency in terms of the relative contribution from the dominant NC02 graphs. In the analyses of $l^+l^-q\bar{q}$ (with $l = e, \mu, \tau$) final states and in one of the two analyses of the $\nu\bar{\nu}q\bar{q}$ final state (the probabilistic selection) described in Sections 5-7, the signal definition used was based on cuts on the generated boson masses, which were required to be within 10 GeV/c^2 of the nominal Z mass [7]. In the other sub-channels, the signal was defined as the sub-set of events satisfying:

$$|\mathcal{M}_{\text{NC02}}|^2 |\mathcal{M}_{\text{All}}|^2 > 0.5,$$

where $\mathcal{M}_{\text{NC02}}$ and $\mathcal{M}_{\text{All}}$ are the values of the matrix elements, computed using the four-momenta of the generated fermions, for NC02 and for all four-fermion graphs, respectively. Corrections were necessary to relate the rates of such events to pure NC02 cross-sections[2], in order to take into account the efficiency of the signal-defining selection cut, the residual contamination from the non-NC02 processes, and interference effects. However, because NC02 and non-NC02 contributions are naturally well separated in phase-space, the magnitudes of these corrections were typically less than a few percent. Simulated four-fermion events which did not satisfy the signal-defining cut were considered as background in the comparison with data.

4   Four jet channel

The $q\bar{q}q\bar{q}$ decay mode represents 48.9% of the expected ZZ final states. It results typically in four or more well separated jets of particles. The dominant backgrounds originate from fully hadronic WW final states and from $q\bar{q}(\gamma)$ processes with hard final state gluon radiation, both of which can lead to similar multi-jet topologies. The main ingredients required to isolate the signal were di-jet mass reconstruction, topological information quantifying the jet separation and kinematics and (for $b\bar{b}q\bar{q}$ decay modes) the b-tagging of the jets. A probabilistic method based on likelihood ratio products was developed to combine in an optimal way the information and compute an event-by-event measure of the compatibility with the ZZ hypothesis, taking into account the flavour content (with or without b-quarks) of the signal.

4.1   Event pre-selection

A pre-selection was applied to select fully hadronic events. Firstly, events were required to contain at least 18 reconstructed tracks of charged particles and to have more than 69% of the available centre-of-mass energy observed in the detector. To reduce the contamination from $q\bar{q}(\gamma)$ processes with energetic photons emitted in the beam pipe, the effective centre-of-mass energy of the event, $\sqrt{s'}$, computed as described in [22], was required to exceed 80% of $\sqrt{s}$. Particles were then clustered into jets using the DURHAM clustering algorithm [23] (with y_{cut}=0.001) and events were selected if at least four jets were reconstructed. To reduce backgrounds from processes with energetic and isolated leptons or photons, jets were required to contain at least four particles and have an invariant mass above 1 GeV/c^2. The efficiency of these cuts was about 88% and 80% for the fully hadronic ZZ signal and WW background, respectively, while about 3% of events from $q\bar{q}(\gamma)$ processes remained. At this stage, backgrounds from all other processes were negligible.

---

[2]Destructive interference from Fermi correlations occurs in the case of final states with four identical fermions [21]. Although modelled by the four-fermion simulation, the resulting reductions in overall cross-section, smaller than 0.5%, were neglected in the calculation of these NC02 cross-sections.

4.2 Probabilistic selection

The method developed enabled the computation of the relative probability for any pre-selected event to originate from each of three SM processes, WW, ZZ or $q\bar{q}(\gamma)$. For this purpose a calculation based on likelihood ratio products was used, based on the main features characterising the ZZ signal: reconstructed di-jet masses, jet kinematics and separation and possible presence of b-hadrons in the jets. These three ingredients and their combination are described below. The computation combined measurements of the events with the theoretical expectations corresponding to each hypothesis, described analytically where possible in order to reduce the dependance on detailed simulations. Throughout the analysis events with four jets and events with five or more jets[3] were treated separately.

Reconstructed mass distributions can be used to characterise the different hypotheses. The expected shapes are well defined, but in reconstructing events ambiguities arise, since in a four or five-jet event, there are three or ten possible jet-jet pairings, respectively. In addition, the quality of the energy flow reconstruction can vary significantly from event to event. Following the scheme described in [24], these considerations were taken into account by simultaneously evaluating the compatibility of each event with each hypothesis considered, WW, ZZ and $q\bar{q}(\gamma)$, from the mass information. For this purpose, probability distributions for the different mass combinations were first expressed in analytical form, as products of Breit-Wigner distributions and phase-space factors to describe the case of correctly paired mass combinations in genuine WW and ZZ events, and as flat spectra for all the other cases. Then, for each reconstructed event, the four-momenta of the jets and their estimated errors were used in kinematic fits [25], requiring four-momentum conservation and equality of the masses of the two jet systems[4] with the pairs of values to be tested. The two-dimensional distributions of the χ^2 probabilities obtained from these fits as a function of the pair of test values were then multiplied by the expected probability distributions and the results integrated to quantify the compatibility of each pairing with each of the WW, ZZ and $q\bar{q}(\gamma)$ hypotheses. To compute global event-level compatibilities with each hypothesis from the mass information, these results were then summed over the possible pairings (assuming equal *a priori* weights) and normalised. As an illustration, the result obtained for the WW hypothesis is shown in the left-hand plot of Figure 2, for the pre-selected events with four jets. In this method, the inherent ambiguity in the pairing of the jets, one of the main difficulties in experimental analyses of multi-jet events, did not need to be resolved.

Specific features of the jet kinematics and separation in events arising from four-fermion and $q\bar{q}(\gamma)$ processes with hard final state gluon radiation leading to a four-jet event were also used. Because gluon emission off quarks has infrared and collinear divergences, these types of events tend to have cigar-like shapes, while the four-fermion processes are more spherical. This difference was exploited to construct a topological variable: $\mathrm{D_{pur}} = E_1\theta_1\sqrt{E_2\theta_2}$, where E_1 (E_2) is the leading (subleading) jet energy and θ_1 (θ_2) is the smallest (next to smallest) opening angle between two jets. The corresponding ratio of probability density functions for these two event types was parametrized as a function of this variable using simulated data for four and five jet events separately. The distribution of the $\mathrm{D_{pur}}$ variable for four-jet events is shown in the right-hand plot of Figure 2.

The presence of b-hadrons in the jets was identified using a dedicated algorithm [26] which exploited their characteristically long lifetime and high mass. This was made

---

[3]Events with more than five jets were forced into a five-jet configuration.

[4]Two di-jets in the case of a four-jet event, and both a di-jet and a three-jet system in the case of a five-jet event.
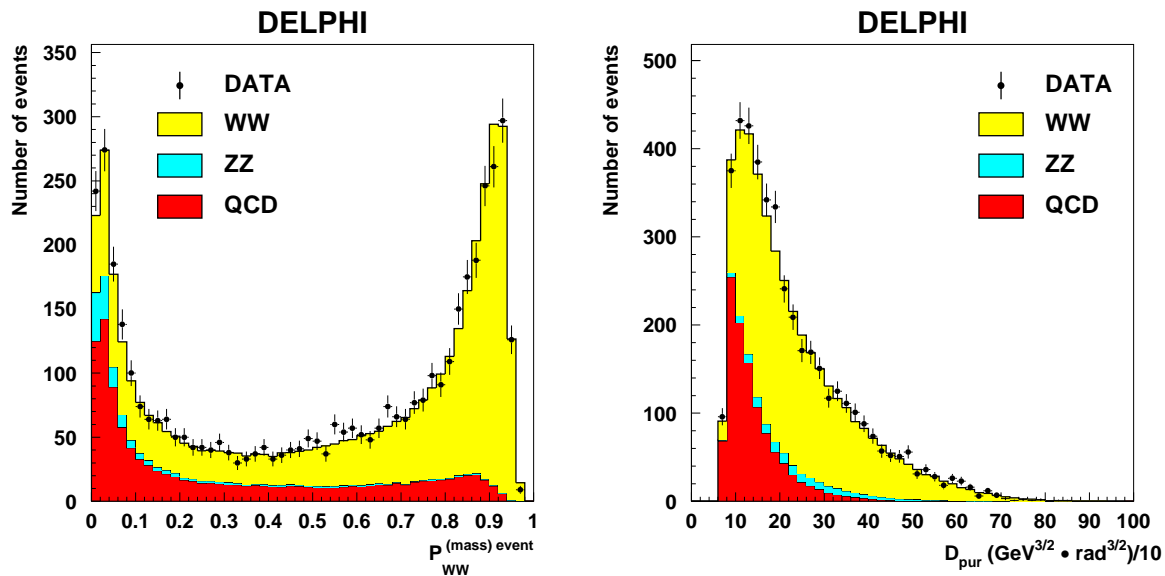
Figure 2: The left-hand plot shows the distribution of the variable quantifying for each event the compatibility with the WW hypothesis, computed using only mass information. The right-hand plot shows the distribution of the event-topology variable D_{pur} (for events with $D_{pur}/10$ greater than 7.5 $GeV^{3/2}rad^{3/2}$). Both distributions are for pre-selected events with four jets (corresponding to about 80% of the total sample). The dots are the data taken in 1997-2000 and the histograms represent the simulation.

possible by the capabilities of the vertex detector [13], in which tracks originating from the displaced b-hadron vertices could be resolved. The combined b-tagging variable which was constructed is shown in Figure 3 for jets in hadronic Z decays (left), and in the pre-selected fully hadronic high-energy event sample (right). It was particularly powerful in reducing the contamination from WW events, since the corresponding final states hardly ever contain a b-quark, while 38.7% of fully hadronic ZZ events have at least two b-quarks. In order to use the information optimally, the ratio of the distributions of this variable for jets originating from the fragmentation of b and non-b quarks was parametrized in three different angular regions, using simulated Z decays, to take into account the polar angle dependence of the detector resolution. Using these parametrizations and the values measured for each jet, relative b and non-b probabilities could be assigned to each jet.

Finally a variable quantifying the compatibility of each event with the ZZ hypothesis was constructed using a method based on likelihood ratio products to combine the information from the different ingredients described. Its distribution is shown in Figure 4, including the data from all centre-of-mass energies. The different energies could be added without diluting the information because the distributions of the purity of ZZ events with respect to the constructed variable were the same.

4.3   Results

As an illustration, the observed and predicted numbers of events selected after a cut on the ZZ probability which maximises the product of efficiency and purity are shown in Table 2. There was an overall agreement between data and simulation within the statistical fluctuations. At each centre-of-mass energy, a measurement of the production
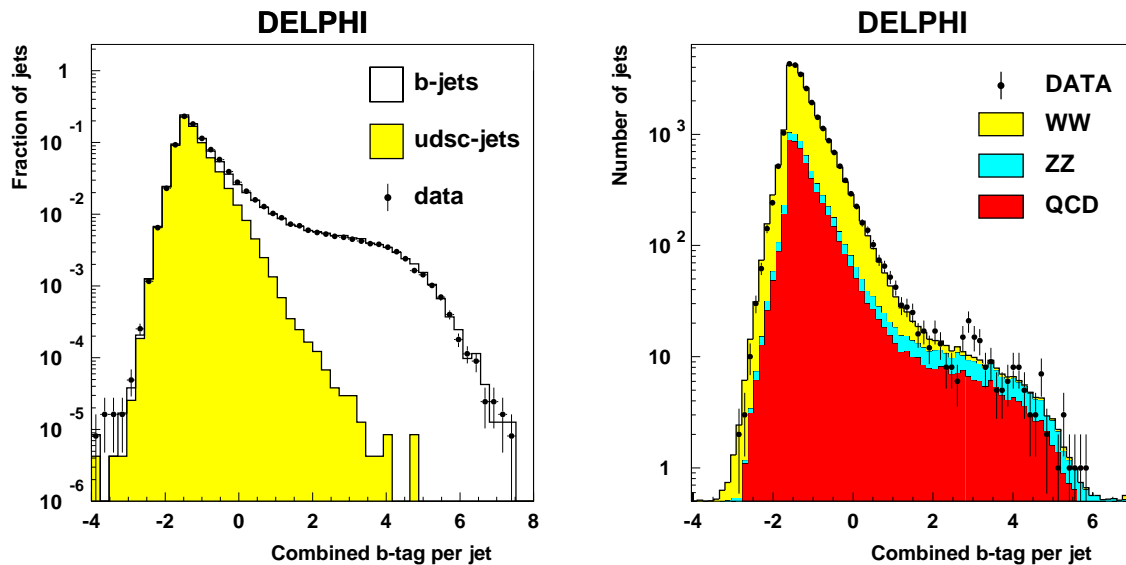
Figure 3: The left-hand plot shows the distribution of the combined b-tagging variable for jets in Z decays collected in special calibration runs during the high-energy data taking. The right-hand plot shows the distribution of the combined b-tagging probability per jet for all reconstructed jets after applying the pre-selection. The dots are the data taken in 1997-2000 and the histograms represent the simulation.

cross-section was obtained from a binned maximum likelihood fit to the distributions of the ZZ probability, with the ZZ signal contribution as the only free parameter. The results obtained and the combinations performed between energies and with other channels to derive global values for the NC02 cross-section are described in Section 10. The optimal region of the ZZ probability distribution to be used in the fit was determined by minimising the combined statistical and systematic uncertainty, evaluated using the full LEP-2 data sample. This resulted in a lower cut on the ZZ probability of 0.25. At this level, the number of events from the WW, $q\bar{q}(\gamma)$ and ZZ processes were comparable.

4.4 Systematic uncertainties

The main source of systematic error in the selection of $ZZ \to q\bar{q}q\bar{q}$ events was from the limited precision available in the modelling of the multi-jet $q\bar{q}(\gamma)$ processes (particularly those involving b-quarks) which comprised the main background in the most signal-like regions relevant to the extraction of ZZ cross-sections. Theoretical uncertainties in the predictions and biases from the generator treatments were studied at $\sqrt{s} = M_Z$, where M_Z is the mass of the Z boson, and extrapolated to LEP-2 energies [27]. The most relevant aspects for the measurement of the $q\bar{q}q\bar{q}$ channel are summarised below.

It was found that PYTHIA [15] underestimated the inclusive four-jet rate[5] by typically about 10% at $\sqrt{s} = M_Z$. The sign and magnitude of this discrepancy were also confirmed by comparisons at LEP-2 energies. After correcting for 1/2 of the discrepancy, $\pm 1/2$ of it was used as a conservative estimate of the uncertainty in the prediction of this rate.

---

[5]The agreement between data and simulation for general hadronic event properties and shapes depends on the strategy applied in the tuning [28] of the generator parameters [27].
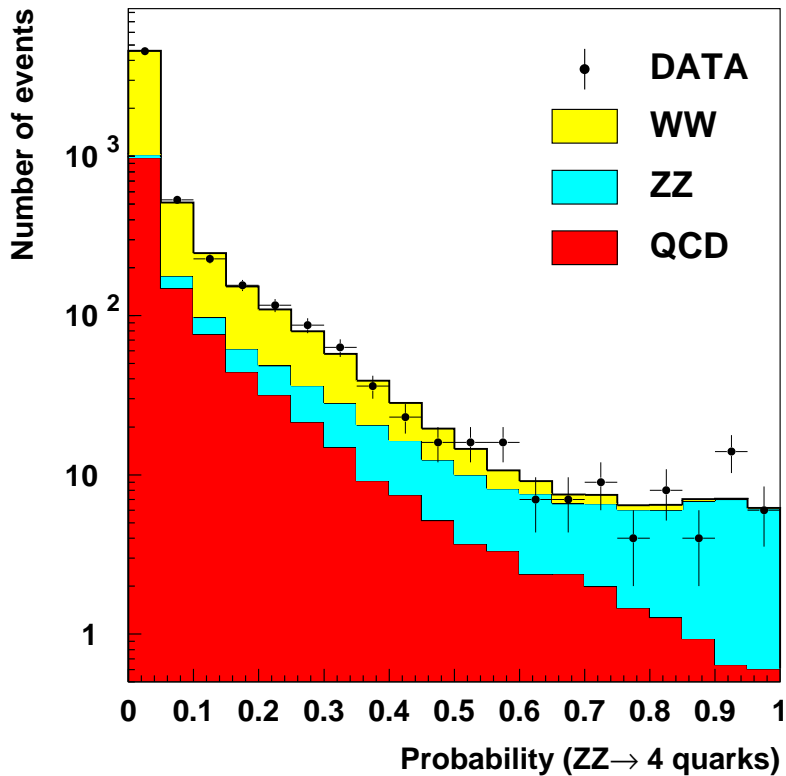
Figure 4: Distribution of the combined ZZ probability. The dots are the data taken in 1997-2000 and the histograms represent the simulation.

The probability of secondary c and b-quark pair production through gluon splitting processes was found to be underestimated in `PYTHIA` by factors of about 1.5 and 2, respectively, compared to other calculations and dedicated measurements. An approximate correction of this deficit was achieved in the analysis by reweighting simulated events containing gluons splitting into heavy quarks with these factors. Since the gluon splitting process remains poorly known both theoretically and experimentally, and since the reweighting procedure applied provided only a rough correction, a $\pm 50\%$ relative error on these probabilities was assumed.

The magnitude of the reduction in gluon radiation off b-quarks relative to other flavours (arising from their heavier mass) was shown to be overestimated in the version of `PYTHIA` used, compared to analytic calculations and to dedicated measurements, typically by as much as the theoretical uncertainty in these calculations. An additional $\pm 4\%$ relative error in the four-jet rate from $q\bar{q}(\gamma)$ processes was conservatively assumed to cover both this uncertainty and bias.

The impact of propagating these uncertainties in the background level to the fitted $ZZ \rightarrow q\bar{q}q\bar{q}$ cross-sections is shown in Table 3, using the full LEP-2 data sample. The effect from uncertainties in selection efficiencies related to the b-tagging procedure is also shown, as well as the effect from varying the WW cross-section within an estimated uncertainty of $\pm 2\%$ [21]. The estimate of the error from b-tagging was obtained by

$ZZ \to q\bar{q}q\bar{q}$					
$\sqrt{s}$ [GeV]	Integrated luminosity [pb^{-1}]	Selection efficiency	Predicted background	Predicted total MC	Selected data
183	54.7	0.13	0.92	1.84	2
189	158.0	0.27	17.88	31.13	29
192	25.9	0.34	5.31	8.64	11
196	76.9	0.38	21.16	34.01	46
200	84.3	0.39	26.64	42.09	36
202	41.1	0.42	14.24	22.55	26
205	82.0	0.41	27.45	43.73	45
207	142.2	0.42	52.58	84.13	78
Total	665.1	0.38	166.18	268.11	273

Table 2: Integrated luminosities, selection efficiencies and number of observed and expected events, after a cut on the probability of the ZZ hypothesis maximising the product of efficiency and purity. The measured ZZ production cross-sections were extracted at each centre-of-mass energy by fitting the distributions of this probability (see the text).

propagating the errors evaluated in [29] to the computed b and non-b jet probabilities. All errors were assumed to be fully correlated between the centre-of-mass energies analysed.

$\sqrt{s}$ [GeV]	Inclusive four-jet rate	Gluon splitting into heavy quarks	Gluon radiation off b-quarks	b-tagging procedure	WW cross-section
183 - 208	±2.3 %	±2.3 %	±1.8 %	±1.5 %	±0.9 %

Table 3: Expected relative uncertainties on the fitted $ZZ \to q\bar{q}q\bar{q}$ cross-section from systematic uncertainties in the predicted background and selection efficiencies.

5   Jets and missing energy

The $\nu\bar{\nu}q\bar{q}$ decay mode represents 28.0% of the ZZ final states. The event topology is characterised by a pair of acoplanar jets (acollinear in the transverse plane to the beam) with visible and recoil masses compatible with the Z mass. Because two energetic neutrinos escape detection in this channel, efficient and reliable energy flow reconstruction is essential to select the signal. The most difficult physical backgrounds arise from single-resonant $We\nu_e$ processes, from WW processes where one W decays into $\tau\nu_\tau$, and from $q\bar{q}$ events, which may or may not be accompanied by energetic isolated photons escaping detection, in which one or both jets are badly reconstructed.

After a common pre-selection, two independent analyses were carried out. Each used a separate selection of discriminating variables to construct a combined estimator, employing different, complementary schemes. The first analysis used a non-linear discriminant method (the so-called Iterative Discriminant Analysis (IDA) [30]) in which the cross-products between the variables were included, and where the correlations - important in this channel - can be treated optimally. The second analysis used a more conventional

probabilistic method based on likelihood ratio products, in which the non-Gaussian profiles of the variables are taken into account. Results from both analyses were obtained and compared. The IDA analysis had slightly better performance, and was chosen to derive the combined values of the NC02 cross-section described in Section 10. It was also used to study the propagation of systematic uncertainties. The probabilistic analysis served as a cross-check.

5.1   Event pre-selection

Selecting carefully the measured particles from which event variables are calculated is important to obtain efficient and reliable energy flow reconstruction. The definition of neutral particles was studied specially in this context, using both energy clusters in the calorimeters not associated to charged particle tracks and reconstructed vertices of photon conversions, of interactions of neutral hadrons and of decays of neutral particles in the tracking volume. Beam related backgrounds were also rejected by requiring at least two charged particles with impact parameter (with respect to the fitted primary vertex) less than 1 mm in the transverse plane and less than 3 mm along the beam axis, and with transverse momentum, P_t, greater than 2 GeV/c. A loose hadronic pre-selection was then applied, requiring at least eight charged particles, total charged energy greater than $0.16\sqrt{s}$, transverse energy (defined as ΣP_t, where the sum is over all particles) greater than $0.15\sqrt{s}$, and the sum of the component of momentum of all particles along the thrust axis greater than $0.25\sqrt{s}$. Finally, events with an electromagnetic shower of energy exceeding $0.45\sqrt{s}$ were rejected. This removed about 97% of the background from two-photon and Bhabha processes.

The particles of the events were forced into two-jet configurations using the DURHAM jet algorithm. To reject events coming from $q\bar{q}(\gamma)$ processes with energetic photons emitted in the beam pipe, the effective centre-of-mass energy of the event, $\sqrt{s'}$, computed from the jet directions, was required to be greater than 115 GeV when the polar angle of the total momentum of detected particles was less than 40° or larger than 140°. To reduce the contamination from $q\bar{q}(\gamma)$ processes with energetic photons in the detector acceptance, events were rejected if their total electromagnetic energy within 30° of the beam axis was greater than $0.16\sqrt{s}$, or if the total energy in the luminosity monitor was greater than $0.08\sqrt{s}$. To reject $q\bar{q}(\gamma)$ processes with energetic photons emitted in blind regions of the electromagnetic calorimetry (at polar angles $\theta \simeq$ 40°, 90° and 140°) signals from the set of dedicated scintillator counters were used. To reduce the two-fermion background without significant initial state radiation as well as four-fermion backgrounds without missing energy, the effective centre-of-mass energy of the event had to satisfy $\sqrt{s'} < 0.96\sqrt{s}$. To reduce backgrounds from two-fermion events with jets pointing to the insensitive regions of the electromagnetic calorimeters, where the energy flow was less precise, events were rejected if the jets had polar angles within the ranges $35 - 45°$ or $135 - 145°$, unless the acoplanarity of the event was greater than 10°. This removed about 88% of the total $q\bar{q}(\gamma)$ background.

The contamination from WW processes where one W decayed leptonically was reduced by requiring that the energy of the most energetic particle of the event be less than $0.2\sqrt{s}$. To improve the rejection when the W decayed into $\tau\nu_\tau$, the events were required to have no charged particle with a transverse momentum with respect to its jet direction greater than 10 GeV/c. This removed about 66% of the WW background.

At the end of the event pre-selection, the efficiency for the $ZZ \rightarrow \nu\bar{\nu}q\bar{q}$ signal was about 77%.

5.2 IDA selection

After the common pre-selection described in Section 5.1, it was additionally required that the momentum of the most isolated particle in the event be in the range $0.01\sqrt{s} < p < 0.20\sqrt{s}$, and that the visible mass be smaller than $\sqrt{s}$. A combined discriminant variable was then constructed using the Iterative Discriminant Analysis program (IDA) [30] to calculate a second order polynomial from twelve event variables, selected according to their discriminating power and independence [6]:

- The logarithm of the transverse momentum of the event with respect to the beam axis, for values greater than 0 (see Figure 5 upper left),
- The visible energy of the event normalised to $\sqrt{s}$, for values lower than 1 (see Figure 5 upper right),
- The transverse energy of the event normalised to $\sqrt{s}$, for values in the range $0.15 - 0.60$,
- The minimum polar angle defining a cone in the positive and negative beam directions containing 6% of the total visible energy,
- The difference of the jet energies normalised to $\sqrt{s}$, for values lower than 0.35,
- The sum of energies of particles having angles with respect to the most isolated particle larger than $5°$ and smaller than $60°$ ($25°$ if the momentum of the most isolated particle exceeded 5 GeV/c), normalised to $\sqrt{s}$, for values lower than 0.15,
- The effective centre-of-mass energy $\sqrt{s'}$,
- The logarithm of the product of the acoplanarity with the inter-jet angle, for values in the range $0.0 - 2.8$ (see Figure 5 lower left),
- The logarithm of the acollinearity of the two jets,
- The longitudinal momentum with respect to the thrust axis, normalised to $\sqrt{s}$, for values lower than 1,
- The missing mass normalised to $\sqrt{s}$, computed with the constraint that the visible mass equal M_Z (see Figure 5 lower right),
- The logarithm of the largest transverse momentum of any particle with respect to its jet direction.

The observed distributions of these twelve variables were in good agreement with the predictions from simulation at each centre-of-mass energy analysed. As an illustration, the distributions of four of them are shown in Figure 5 after all pre-selection cuts, for $\sqrt{s} = 199.5$ GeV. The IDA method for variable combination was applied in two successive optimisations. Following the first one, an enriched sub-sample of events was selected, with a 95% relative signal efficiency. These events were then used in the second optimisation. The final combined discriminant variable obtained is shown in the left-hand plot of Figure 6, including the data from all centre-of-mass energies.

5.3 Probabilistic selection

After the common pre-selection described in Section 5.1, it was additionally required that the total visible energy be lower than $0.70\sqrt{s}$. A probabilistic method based on likelihood ratio products was then used to combine nine discriminating variables:

- The energy of the most energetic jet,
- The cosine of the acoplanarity,

---

[6]To concentrate on the signal region when optimizing the second-order discriminant function, and to avoid long non-Gaussian tails, additional very loose pre-selection cuts were applied to some of the variables, as indicated in the description.
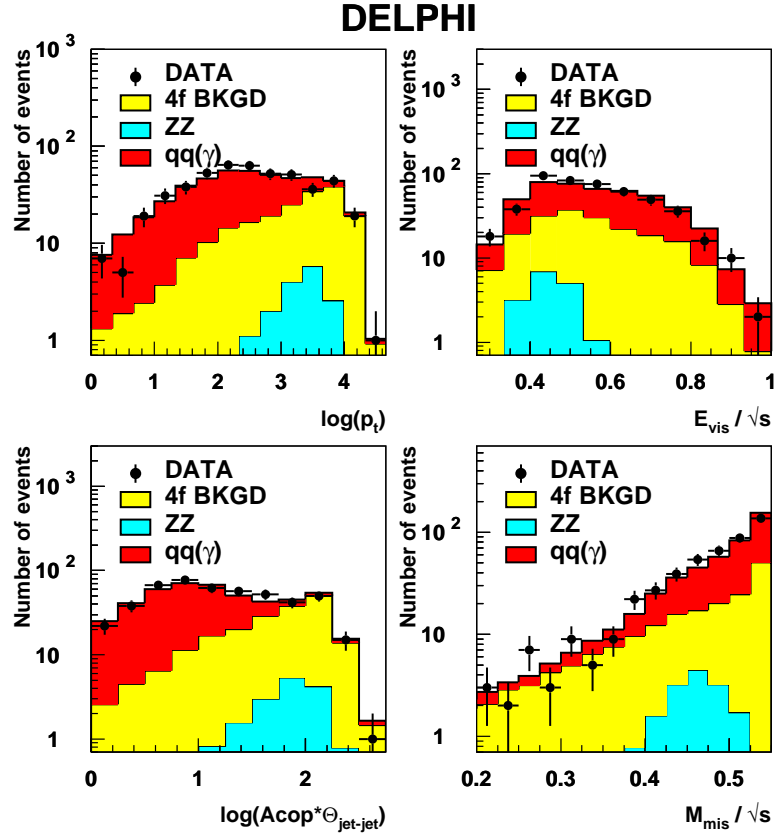
Figure 5: Distributions of four variables used in the IDA analysis stream shown after all pre-selection cuts (see text): logarithm of the transverse momentum (in GeV/c) with respect to the beam axis (upper left), ratio of the visible energy to the centre-of-mass energy (upper right), logarithm of the product of the inter-jet angle (in degrees) and the acoplanarity (lower left), ratio of the missing mass (computed using the constraint that the visible mass be compatible with M_Z) to the centre-of-mass energy (lower right). The dots are the data taken in 1999 at a centre-of-mass energy $\sqrt{s} = 199.5$ GeV. The histograms are the simulation prediction.

- The effective centre-of-mass energy $\sqrt{s'}$, normalised to $\sqrt{s}$,
- The missing momentum,
- The cosine of the polar angle of the missing momentum,
- The largest transverse momentum of any particle with respect to its jet direction,
- The minimum charged multiplicity of the jets[7],
- The visible mass, computed with the constraint that the missing mass equal M_Z,
- The output of a veto algorithm based on the response of the dedicated scintillator counters installed at polar angles $\theta \simeq 40°$, $90°$ and $140°$.

There was good agreement between the data and the predictions from the simulation for each of these variables at each centre-of-mass energy. The probability density functions used to construct the combined discriminant variable were determined from the

---

[7]In this case events were not forced into two-jet configurations and the DURHAM jet clustering algorithm was used with $y_{cut} = 0.005$.
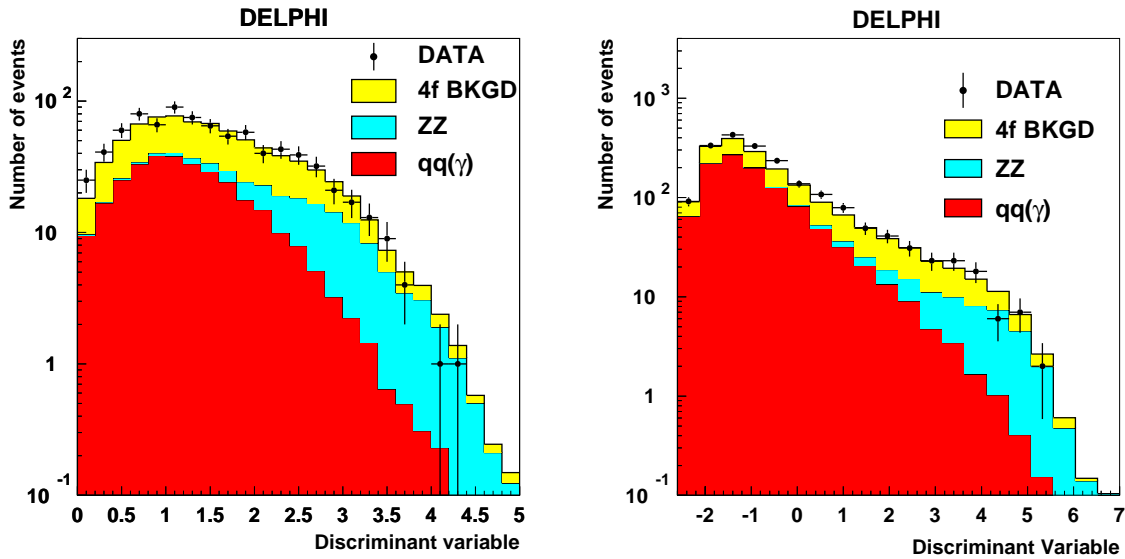
Figure 6: Distribution of the combined discriminating variable for the $\nu\bar{\nu}q\bar{q}$ analysis in the IDA (left) and probabilistic (right) selections. The dots are the data taken in 1997-2000 and the histograms represent the simulation. The distributions of the purity of ZZ events as a function of these two variables were almost identical for all centre-of-mass energies, allowing to add the histograms of the different energies with minimal dilution of the information.

simulation, separately at each energy. The distribution of this final variable is shown in the right-hand plot of Figure 6, including the data from all centre-of-mass energies.

5.4   Results and comparison

The results from the two selections are presented in Table 4, where the observed and predicted numbers of events, selected after cuts on each discriminant variable maximising the product of the efficiency and purity, are shown[8]. The two methods gave compatible results, but the IDA selection performed slightly better. There was overall agreement between data and simulation within statistical errors in both cases. A study of the overlap between the two selections, performed with the data collected in 2000, showed that the proportion of common events was about 60% in real data: 55% in the background and 85% in the signal, according to the simulation. The IDA selection was used as the main analysis, and the probabilistic as cross-check.

At each centre-of-mass energy, a measurement of the production cross-section was obtained from a binned maximum likelihood fit to the distribution of the final IDA variable, with the ZZ signal contribution as the only free parameter. The results obtained and the combinations performed between energies and with other channels to derive global values for the NC02 cross-section are described in Section 10. The optimal region of the distribution of the IDA variable to be used in the fit was determined by minimising the combined statistical and systematic uncertainty, evaluated using the full LEP-2 data sample. This resulted in removing events with values of the IDA variable less than

---

[8]The luminosities used to analyse the $ZZ \to \nu\bar{\nu}q\bar{q}$ channel were slightly lower than for other channels, because additional criteria on the operation of the apparatus were used.

$ZZ \to \nu\bar{\nu}q\bar{q}$ (IDA selection)					
$\sqrt{s}$ [GeV]	Integrated luminosity [pb^{-1}]	Selection efficiency	Predicted background	Predicted total MC	Selected data
183	52.4	0.31	1.6	3.1	2
189	152.8	0.49	14.8	28.3	22
192	24.9	0.56	5.1	8.1	6
196	75.0	0.52	13.3	22.6	27
200	82.2	0.56	18.7	31.0	25
202	40.4	0.48	7.5	13.0	12
205	72.9	0.54	16.8	27.9	22
207	138.4	0.52	30.7	51.9	49
Total	639.0	0.50	108.5	185.9	165

$ZZ \to \nu\bar{\nu}q\bar{q}$ (Probabilistic selection)					
$\sqrt{s}$ [GeV]	Integrated luminosity [pb^{-1}]	Selection efficiency	Predicted background	Predicted total MC	Selected data
183	52.4	0.27	1.8	3.1	4
189	152.8	0.46	24.3	36.7	32
192	24.9	0.50	5.6	8.5	9
196	75.0	0.46	12.7	21.4	20
200	82.2	0.46	16.4	26.0	25
202	40.4	0.51	10.9	16.6	16
205	72.9	0.48	18.0	28.4	24
207	138.4	0.45	29.6	47.6	48
Total	639.0	0.45	119.3	188.3	178

Table 4: Integrated luminosities, selection efficiencies and number of observed and expected events in the $ZZ \to \nu\bar{\nu}q\bar{q}$ channel, after cuts on each discriminant variable maximising the product of the efficiency and purity. In the IDA analysis, the measured ZZ production cross-sections were extracted at each centre-of-mass energy by fitting the distributions of the corresponding discriminant variable (see the text).

2.2. The cross-section measured by combining the results of the probabilistic cross-check analysis over the different energies is also given in Section 10 for comparison, using the numbers of events and efficiencies presented in Table 4.

The remaining background was composed of several processes. Near the threshold for ZZ production, the main backgrounds were from $q\bar{q}(\gamma)$ events with badly reconstructed jets, and from WW processes. At higher energies, mis-reconstructed $q\bar{q}(\gamma)$ events were easier to suppress, due to the Lorentz boost of the Z bosons in the signal. In this case, the main background was from single-resonant $We\nu_e$ processes.

5.5   Systematic errors

The main sources of systematic error in the selection of $ZZ \to \nu\bar{\nu}q\bar{q}$ events were from uncertainties in the description of the energy flow reconstruction of the $q\bar{q}(\gamma)$ background and, to a lesser extent, from uncertainties in the predicted background cross-sections, particularly those of the single-resonant $We\nu_e$ process. The propagation of these uncertainties to the final steps of the IDA analysis was studied.

Large samples of events at the Z peak, collected in the same conditions as the high energy data, were used to evaluate the errors in the energy flow reconstruction. The selection of $ZZ \to \nu\bar{\nu}q\bar{q}$ events exploits the large missing energy characteristic of this channel, and hence is sensitive to the description of the low energy tail in the reconstruction of background processes such as $q\bar{q}(\gamma)$. The Z events were compared with the simulation to estimate corrections to the particle flow in several momentum bins, separately for the barrel and endcaps, and for charged and neutral particles. The corrections, consisting mainly of changes in multiplicities to account for observed efficiency losses and possible duplication effects in the pattern recognition, were typically only a few per cent for charged particles, but could be larger in the case of neutral particles at low momentum or in the endcaps. It was found that the simulation overestimated particle reconstruction efficiencies in the highest momentum bins. This resulted in underestimating the lower tail of the total energy distribution. Application of the computed corrections significantly improved the overall agreement between data and simulation at the pre-selection level for all energy flow observables such as the total charged and neutral energies, the visible mass or the acoplanarity. Partial improvement also resulted in the tails of the distributions most relevant to the selection of $ZZ \to \nu\bar{\nu}q\bar{q}$ events, although comparisons were in this case limited by the statistics of the available samples.

This correction procedure was then applied to all simulated high energy samples and the IDA analysis was repeated. The main effect was to increase the $q\bar{q}(\gamma)$ background in the high purity regions relevant to the signal extraction by about one third on the average, while other components were much less affected. The ZZ cross-sections were then fitted, at each centre-of-mass energy, using these modified versions of the simulation. The differences in expected results were always of the same sign, corresponding to reductions in the ZZ cross-section obtained. After correcting for $1/2$ of these discrepancies, $\pm 1/2$ of them were used as conservative estimates of the errors resulting from uncertainties in the energy reconstruction. The magnitude of the effects decreased with energy, because of the decreasing relative importance of the $q\bar{q}(\gamma)$ background.

The impact of propagating these uncertainties in the energy reconstruction to the fitted $ZZ \to q\bar{q}\nu\bar{\nu}$ cross-sections is shown in Table 5, using the full LEP-2 data sample. The combined effect from uncertainties in background cross-sections is also shown, assuming the following errors [21]: $WW : \pm 2\%$, $We\nu : \pm 5\%$, $q\bar{q}(\gamma) : \pm 2\%$. Both types of error were assumed to be fully correlated between the energies analysed.

$\sqrt{s}$ [GeV]	Systematic error from energy flow	Systematic error from MC cross-sections
183	± 14.5 %	± 4.0 %
189	± 10.0 %	± 2.5 %
192	± 7.5 %	± 2.5 %
196 - 208	± 3.5 %	± 2.5 %

Table 5: Expected effects on the $ZZ \to \nu\bar{\nu}q\bar{q}$ cross-section fitted in the IDA analysis, from uncertainties in the energy flow reconstruction and predicted background cross-sections.

6   Jets and a pair of isolated muons or electrons

The $\mu^+\mu^-q\bar{q}$ and $e^+e^-q\bar{q}$ decay modes comprise 9.3% of the ZZ final states. The two final state leptons are typically well isolated from all other particles. This feature can be used to select such events with high efficiency and low background contamination in both the muon and electron channels. Events were selected initially without explicit cuts on the masses of the final state fermion pairs, in order to analyse simultaneously the production of ZZ and $Z\gamma^*$ events and, in the case of the $e^+e^-q\bar{q}$ channel, contributions from the $(Z/\gamma^*)e^+e^-$ process. Mass cuts were then applied to isolate the ZZ contribution.

6.1   Selection procedure

A loose hadronic pre-selection was first applied, requiring that the events have at least 7 charged particles and a charged energy above $0.30 \sqrt{s}$. To reduce the radiative return to the Z boson, events were rejected if a photon with energy greater than 60 GeV was found. The selection procedures were then closely similar for both $\mu^+\mu^-q\bar{q}$ and $e^+e^-q\bar{q}$ channels. In order to maximize the lepton identification efficiency, any charged particle with momentum exceeding 5 GeV/c was considered as a possible lepton candidate, around which nearby photons, if present, could be clustered[9]. This was found necessary to improve its energy evaluation in the presence of final state radiation. In the case of the $e^+e^-q\bar{q}$ channel, photons with energy between 20 GeV and 60 GeV were also considered as possible electron candidates, to recover events in which the electron track was not reconstructed.

Events with at least two lepton candidates of the same flavour, opposite charge (if none of the electron candidates originated from a photon) and invariant mass exceeding 2 GeV/c^2 were then selected. All particles except the lepton candidates were clustered into jets using the JADE algorithm [31] (with $y_{min} = 0.01$) and a kinematic fit requiring four-momentum conservation was applied, correcting appropriately the errors on lepton energies in cases where photons had been added by the clustering procedure.

At least one of the two lepton candidates was required to satisfy strong lepton identification criteria, while weaker requirements were specified for the second. Muons were considered as strongly identified if selected by the standard DELPHI muon identification package [12], based mainly on finding associated hits in the muon chambers. For weak muon identification only a set of kinematic and calorimetric criteria was used. Electrons were considered as strongly identified when the energy deposited in the electromagnetic

---

[9]For this purpose any neutral particle identified as a photon with energy greater than 0.5 GeV was combined with the lepton candidate if the invariant mass of the resulting cluster did not exceed 0.4 GeV/c^2. At most two photons were included in such a cluster, the photon giving the smallest mass increase being added first.

calorimeter exceeded 15 GeV or 60% of the total energy of particles composing the electron candidate cluster and when the energy deposited in the hadron calorimeter was consistent with the expectations for electrons. For weak electron identification only requirements on the momentum of the charged particle in the cluster and on the energy deposited in the hadron calorimeter were used. Moreover electron candidates originating from applying the clustering procedure around a photon were considered as weakly identified.

Two discriminating variables were then used to select the events: P_t^{min}, the lesser of the transverse momenta of the lepton candidates with respect to their nearest jet, and the χ^2 per degree of freedom of the kinematic fit.

6.2   Results

The distribution of the mass of one fermion pair (M_{ll} or $M_{q\bar{q}}$) when the mass of the second pair is within $15 \, \mathrm{GeV}/c^2$ of the nominal Z mass is shown in Figure 7 (upper left and right-hand plots, respectively) for the selected events. The corresponding distribution of the sum of the masses of the two fermion-pairs is shown in the lower plot of Figure 7. The observed distributions are in reasonable agreement with the predictions from simulation. To select on-shell ZZ production, cuts were placed simultaneously on the masses of the l^+l^- pair, on the remaining hadron system and on their sum, taking into account in the performance optimization the different mass resolutions of these final states and the presence of the single-resonant process, e^+e^-Z, in the case of the $e^+e^-q\bar{q}$ channel. The observed and predicted numbers of selected on-shell ZZ events are shown in Table 6. The residual background is composed of $l^+l^-q\bar{q}$ events generated outside the signal region (see Section 3), of other processes, principally W^+W^-, other ZZ decays and, in the case of $e^+e^-q\bar{q}$, $q\bar{q}(\gamma)$ production. These results were used to derive the combined values of the NC02 cross-section described in Section 10.

6.3   Systematic errors

Several possible sources of systematic errors were checked. Uncertainties in the efficiency of the lepton identification were studied comparing semileptonic WW events selected in data and simulation using the strong lepton identification criteria. Uncertainties in signal efficiencies from the description of the kinematic observables used were evaluated comparing the P_t and χ^2 distributions in data and simulation for all $l^+l^-q\bar{q}$ events selected without mass cuts. Corresponding uncertainties in background levels were evaluated by comparing samples of events selected in data and in simulation, requiring both isolated tracks to be not identified as leptons, while maintaining all the other criteria. Finally, uncertainties in the background level in the $e^+e^-q\bar{q}$ channel from fake electrons were studied with $q\bar{q}(\gamma)$ events selected in data and in simulation with purely kinematic criteria. These effects and the statistical uncertainty of simulated data yielded combined systematic errors on the efficiency to select $\mu^+\mu^-q\bar{q}$ and $e^+e^-q\bar{q}$ events of $\pm3.0\%$, and on the relative uncertainty in the background level of $\pm15\%$[10]. Finally, additional errors of $\pm2\%$ and $\pm3\%$ were added in the procedure to extract and combine the cross-sections with other channels (see Section 10), to account for uncertainties from the signal definition used (see Section 3), arising partly because of interference effects and because of biases resulting from the single-resonant $(Z/\gamma^*)e^+e^-$ process, respectively.

---

[10]These evaluations were limited in accuracy by the statistics of the available samples.

$\sqrt{s}$ [GeV]	Integrated luminosity [pb^{-1}]	Selection efficiency	Predicted background	Predicted total MC	Selected data
$ZZ \to \mu^+\mu^- q\bar{q}$					
183	54.0	0.88	0.04	0.52	3
189	158.1	0.87	0.22	4.14	5
192	25.8	0.89	0.05	0.91	0
196	76.9	0.88	0.12	2.71	1
200	84.3	0.87	0.15	3.20	5
202	41.1	0.84	0.08	1.62	0
205	83.3	0.87	0.17	3.34	2
207	141.8	0.84	0.30	5.70	5
Total	665.3	0.86	1.13	22.14	21
$ZZ \to e^+e^- q\bar{q}$					
183	54.0	0.72	0.18	0.73	0
189	158.1	0.74	0.64	4.19	3
192	25.8	0.75	0.13	0.93	1
196	76.9	0.74	0.36	2.73	4
200	84.3	0.74	0.45	3.27	2
202	41.1	0.72	0.17	1.50	1
205	83.3	0.74	0.34	3.30	4
207	141.8	0.70	0.55	5.37	4
Total	665.3	0.73	2.82	22.02	19

Table 6: Integrated luminosities, selection efficiencies and number of observed and expected selected events in the $ZZ \to \mu^+\mu^- q\bar{q}$ and $ZZ \to e^+e^- q\bar{q}$ channels.
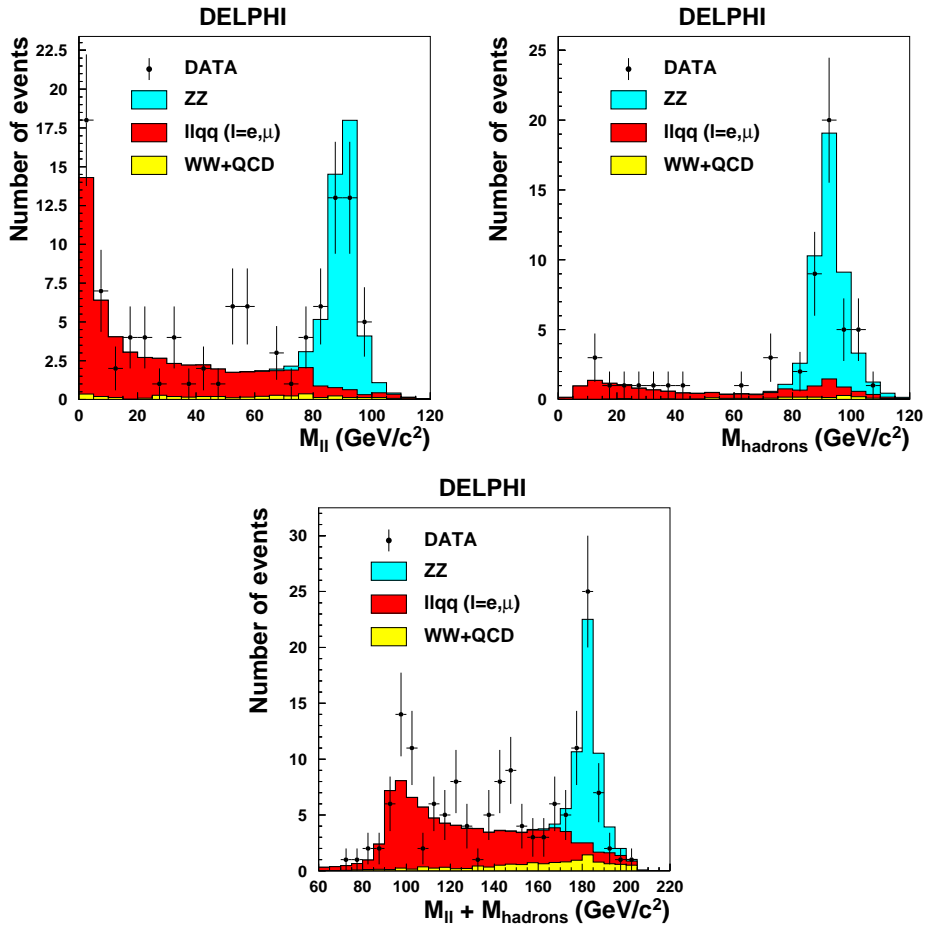
Figure 7: Distribution of the mass of the lepton pair (hadron system) when that of the hadron system (lepton pair) is within 15 GeV/c^2 of the nominal Z mass (upper left and right-hand plots, respectively) and of the sum of the masses of the lepton pair and hadron system (lower plot) for the selected events. The dots are the data taken in 1997-2000 and the histograms represent the simulation. The background labelled $l^+l^-q\bar{q}$ ($l = e, \mu$) corresponds to the predicted contributions from these final states not satisfying the signal definition described in Section 3.

7   Jets and a pair of isolated τ-leptons

The $\tau^+\tau^-q\bar{q}$ decay mode represents 4.7% of the ZZ final states. The search for $\tau^+\tau^-q\bar{q}$ final states was based on the inclusive selection of isolated clusters of particles with low charged multiplicity and low invariant mass. Each pair of such clusters was considered as a possible $\tau^+\tau^-$ candidate, with all other particles assumed to originate from a $q\bar{q}$ system. Assuming this topology, a set of discriminating variables reflecting the isolation of the clusters and the likelihood of the $\tau^+\tau^-q\bar{q}$ hypothesis was defined. All these variables were combined into a single quantity using a probabilistic method based on likelihood ratio products. Cutting on this combined variable enabled $\tau^+\tau^-q\bar{q}$ final states consistent with ZZ production to be selected with high efficiency and low background contamination.

7.1 Definition of τ-clusters

Each charged particle with momentum exceeding 1 GeV/c was considered as a τ-cluster candidate. Every other charged particle (with energy exceeding 1 GeV) and photon (with energy exceeding 0.5 GeV) was then successively added to each one of these candidates and the incremental change in the cluster mass ΔM_{cl} was computed. After sorting the particles in increasing order of ΔM_{cl}, the particle which produced the minimal ΔM_{cl} was kept if the charged and neutral particle cluster multiplicities were each less than 4, if ΔM_{cl} was less than 1.5 GeV/c^2 and, for clusters with one (more than one) charged particle, if their mass, M_{cl}, was less than 2.5 (1.9) GeV/c^2.

After adding each particle, the determination of ΔM_{cl} was repeated for all remaining particles with the modified cluster. The procedure was continued until all combinations had been tried. If the initial charged particle was identified as an electron or a muon (using the standard packages described in [12]), only photons were added. To study the isolation of these τ-cluster candidates, all the particles of the events were clustered into jets with the JADE algorithm [31] (using $y_{min} = 0.01$). The four-momenta of the tracks of the τ-cluster were subtracted from the jets to which they belonged, and the nearest jet with a remaining energy exceeding 3 (1.5) GeV, for a cluster with one (more than one) charged particle, was determined. Two variables characterising the isolation of each cluster were defined: the angle θ_{cl} between the cluster and the nearest jet, and the transverse momentum P_t of the most energetic particle in the cluster with respect to the nearest jet.

7.2 Pre-selection

Events were required to have at least 7 reconstructed charged particles and a charged energy greater than 0.30 $\sqrt{s}$. To suppress radiative returns to the Z, events were rejected if a photon with energy exceeding 55% of the beam energy was found. At least two τ-clusters per event were required, satisfying the isolation criterion $\cos\theta_{cl} < 0.95$ (0.92), for clusters with one (more than one) charged particle, having a sum of charges satisfying the condition $|Q_1 + Q_2| < 2$, and with at least one of these clusters containing only one charged particle.

All particles not used to define the two τ candidates were then clustered into jets and a kinematic fit [25] with six constraints, consisting of four-momentum conservation and imposition of the condition $M_{\tau^+\tau^-} = M_{q\bar{q}} = M_Z$, was applied to the event, where $M_{\tau^+\tau^-}$ and $M_{q\bar{q}}$ are the invariant masses of the τ and jet systems, respectively. To exploit the large missing energy in the τ decay, the missing energies of each τ-cluster, $D_E^{1,2}$ (defined as the differences between each fitted cluster energy, $E_{fit}^{1,2}$, and the corresponding measured value), were then required to satisfy:

- $\min(D_E^1, D_E^2) > -15$ GeV,
- $\min(D_E^1, D_E^2) > 10$ GeV if the clusters contained identified leptons (electrons or muons) of the same type,
- $D_E^i > 3$ GeV $(i = 1, 2)$ for τ-clusters containing an identified lepton,
- $D_E^1 + D_E^2 > 10$ GeV if one or both τ-clusters contained an identified lepton.

After all these pre-selection criteria, the total number of events observed in data and predicted in simulation were 505 and 460.7, respectively.

7.3 Probabilistic selection

A probabilistic method based on likelihood ratio products was used to combine several variables defined at the level of the τ-clusters ($E_{fit}^{1,2}$, $D_E^{1,2}$, $\cos\theta_{cl}^{1,2}$, $P_t^{1,2}$), and the χ^2 probabilities of three kinematic fits, performed using the constraints from four-momentum conservation, using in addition the hypothesis of ZZ production (as described in section 7.2) or that of WW production (requiring the two di-jet masses reconstructed in the pairing with smallest χ^2 to be equal to M_W). The probability density functions were determined for each quantity by combining the predictions from all centre-of-mass energies separately for τ-clusters with leptons, with one charged particle and with more than one charged particle. The separation power of Y, the combined discriminant variable obtained, is illustrated in Figure 8, where the distribution of $-\log_{10} Y$ is shown for a sample enriched with signal events by requiring $M_{\tau^+\tau^-}$ and $M_{q\bar{q}}$ to be compatible with the Z boson mass.
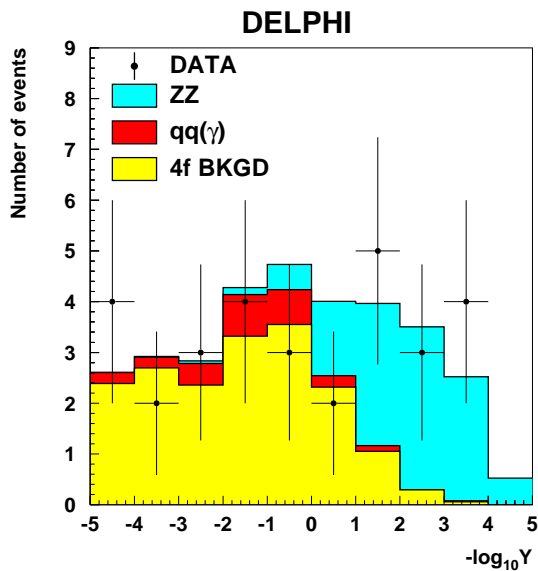
Figure 8: Distribution of the combined discriminating variable for the $\tau^+\tau^- q\bar{q}$ analysis, obtained after enriching with signal events by requiring $M_{\tau^+\tau^-}$ and $M_{q\bar{q}}$ to be compatible with the Z boson mass. The dots are the data taken in 1997-2000 and the histograms represent the simulation.

7.4 Results

To isolate the on-shell ZZ production process, a cut, chosen to maximise the product of the efficiency and purity, was applied to the combined variable: $-\log_{10} Y > 0.5$. The fermion pair mass distributions for the events selected by this cut ($M_{\tau^+\tau^-}$ and $M_{q\bar{q}}$) are shown in Figure 9, obtained after a kinematic fit of the event with the constraints from four-momentum conservation only. The observed distributions are in reasonable agreement with the predictions from simulation. Additional mass cuts were used to improve the signal-to-background ratio for the final selection: $75 < M_{\tau^+\tau^-, q\bar{q}} < 110$ GeV/c^2 and $170 < M_{\tau^+\tau^-} + M_{q\bar{q}} < 200$ GeV/c^2. The observed and predicted numbers of selected events are shown in Table 7. The background is composed of $q\bar{q}q\bar{q}$, $(e^+e^-, \mu^+\mu^-)q\bar{q}$ and

$q\bar{q}(\gamma)$ events. The $q\bar{q}q\bar{q}$ final states were primarily from WW decays. The overall contribution from other ZZ decays was less than 30% of the total background. These results were used to derive the combined values of the NC02 cross-section described in Section 10.
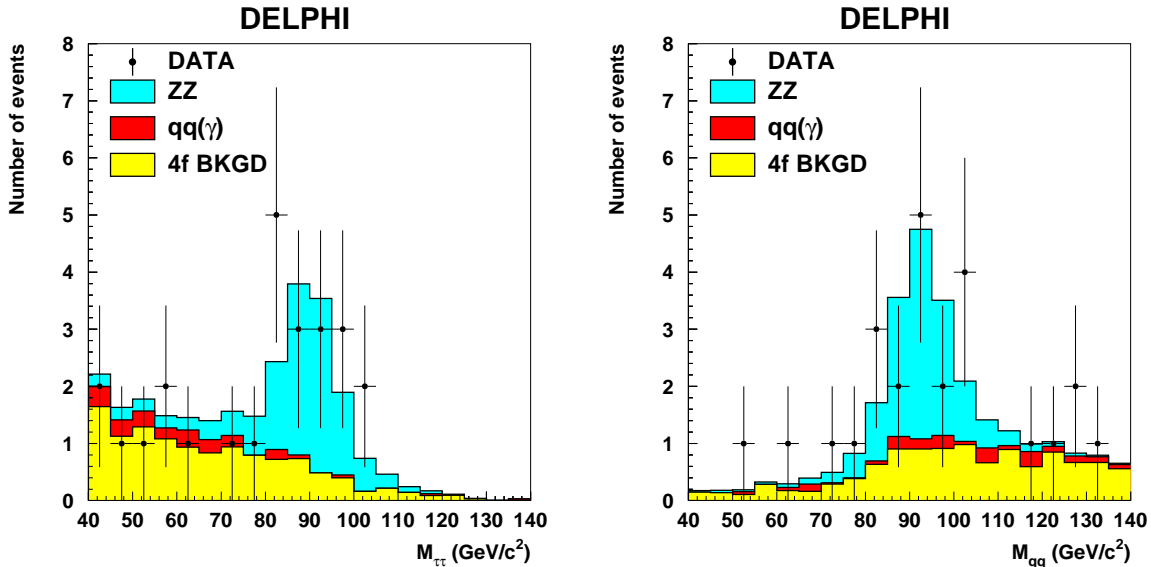

Figure 9: Distribution of $M_{\tau^+\tau^-}$ and $M_{q\bar{q}}$, obtained through kinematic fitting of the event with the constraints from four-momentum conservation only, for the selected events satisfying $-\log_{10} Y > 0.5$ (see the text). The dots are the data taken in 1997-2000 and the histograms represent the simulation.

7.5   Systematic errors

The main sources of systematic error in the selection of $ZZ \to \tau^+\tau^- q\bar{q}$ events arose from uncertainties in the reconstruction of the τ-clusters and associated isolation variables. After the pre-selection, about 10% more events were selected in data as compared to Monte Carlo (see Section 7.2). At this level the selection is dominated by WW processes where one W decays into $\tau\nu_\tau$ and the other into hadrons. Although the corresponding topology is not identical with that of the signal, it is similar since it contains a τ-lepton to be identified in the presence of hadronic jets. A systematic uncertainty of $\pm 10\%$ on the selection efficiency was assigned to take this discrepancy into account and based on studies of uncertainties in the lepton identification used in the selection of the τ-clusters. An uncertainty in the background level of $\pm 30\%$ was also specified because the fraction of background events originating from other ZZ decays (see Section 7.4) was neglected in the procedure to derive combined NC02 cross-sections. Both errors were assumed to be fully correlated between the centre-of-mass energies analysed.

$\sqrt{s}$ [GeV]	Integrated luminosity [pb^{-1}]	Selection efficiency	Predicted background	Predicted total MC	Selected data
		$ZZ \to \tau^+\tau^- q\bar{q}$			
183	54.0	0.28	0.09	0.28	0
189	158.1	0.34	0.52	2.08	1
192	25.8	0.40	0.12	0.49	0
196	76.9	0.41	0.32	1.56	0
200	84.3	0.41	0.42	1.91	1
202	41.1	0.41	0.20	0.94	2
205	83.3	0.41	0.38	1.91	4
207	141.8	0.40	0.64	3.26	5
Total	665.3	0.38	2.69	12.43	13

Table 7: Integrated luminosities, selection efficiencies and number of observed and expected selected events in the $ZZ \to \tau^+\tau^- q\bar{q}$ channel, after cuts on $M_{\tau^+\tau^-}$, $M_{q\bar{q}}$ and on their sum.

8   Final states with four charged leptons

The $l^+l^-l^+l^-$ decay modes with $l = e, \mu$ comprise 0.4% of the ZZ final states. The event topology is clean and the only significant background comes from non-resonant $e^+e^-l^+l^-$ production.

8.1   Selection procedure

Events were first selected if they contained between 4 and 8 charged particles, accompanied by at most 10 neutral particles, irrespective of particle identification. In order to take into account bremsstrahlung effects for candidate electrons, the momentum of a charged particle was replaced by the sum of energies of electromagnetic clusters in a narrow cone around the track direction if it gave a larger value. The total invariant mass of the charged particles had to be greater than 50 GeV/c^2, and the minimum invariant mass after discarding any one of the charged particles larger than 20 GeV/c^2. All combinations of four charged particles with total charge zero were then examined, and a combination was selected if all the following criteria were satisfied:

- all four tracks had impact parameters at the interaction point smaller than 3.0 and 0.5 cm, respectively in the projections containing the beam axis and perpendicular to it, and polar angles between 10° and 170°,
- at least three of the four charged particles had momenta greater than 5 GeV/c, and the least energetic particle had momentum greater than 2 GeV/c,
- a system of two oppositely charged particles was found with both their invariant and missing masses within 10 GeV/c^2 of the Z boson mass and having the same flavour (when both were identified as either electrons or muons using the standard packages described in [12]),
- the two particles complementary to this system were separated by at least 90° from each other,

- the invariant mass of all pairs of oppositely charged particles in the event exceeded 5 GeV/c^2.

8.2 Results

The observed and predicted numbers of selected events are shown in Table 8. They are in overall agreement within the statistical errors. These results were used to derive the combined values of the NC02 cross-section described in Section 10. The two events selected at $\sqrt{s} = 188.6$ and 199.5 GeV were in the $\mu^+\mu^-e^+e^-$ and $\mu^+\mu^-\mu^+\mu^-$ final states, respectively. An event display for the latter is shown in Figure 10.

$ZZ \to l^+l^-l^+l^-$					
$\sqrt{s}$ [GeV]	Integrated luminosity [pb^{-1}]	Selection efficiency	Predicted background	Predicted total MC	Selected data
183	54.0	0.53	0.09	0.17	0
189	158.1	0.62	0.15	0.76	1
192	25.8	0.58	0.06	0.19	0
196	76.9	0.54	0.13	0.47	0
200	84.3	0.54	0.17	0.60	1
202	41.1	0.54	0.07	0.27	0
205	83.3	0.50	0.22	0.62	0
207	141.8	0.41	0.28	0.84	0
Total	665.3	0.53	1.17	3.92	2

Table 8: Integrated luminosities, selection efficiencies and number of observed and expected selected events in the $ZZ \to l^+l^-l^+l^-$ channel.

8.3 Systematic errors

The main sources of systematic error in the analysis of the $ZZ \to l^+l^-l^+l^-$ decay modes with $l = e, \mu$ were from the statistics of the Monte Carlo samples produced to compute the residual background and the selection efficiency and from approximations used to translate the results in terms of NC02 cross-sections (see Section 3). These three uncertainties were propagated into the combination described in Section 10. They amounted to $\pm 12\%$, $\pm 5\%$ and $\pm 5\%$ relative errors on the cross-sections obtained in this channel, respectively, and dominated over uncertainties in background cross-sections and reconstruction. The third error was assumed to be fully correlated between the energies analysed.

9 Two isolated electrons or muons with missing energy

The $\nu\bar{\nu}l^+l^-$ decay modes with $l = e, \mu$ comprise 2.7% of the ZZ final states. The events are characterized by two acollinear charged leptons of the same flavour, with both
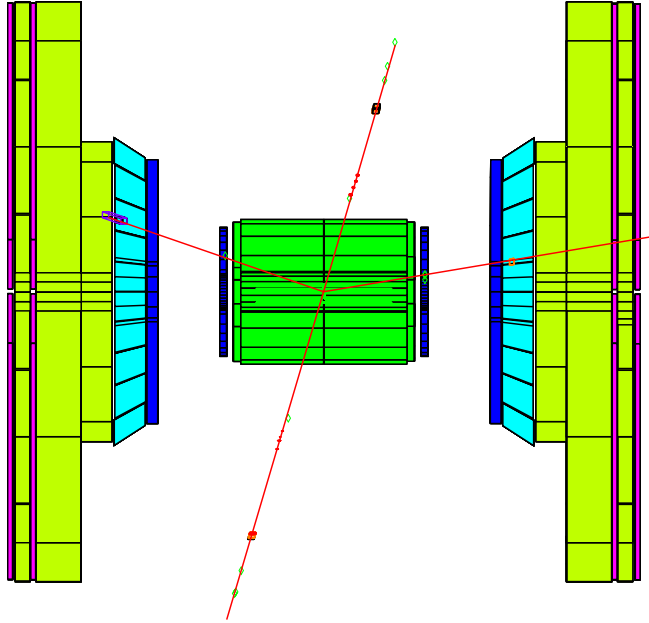
Figure 10: The $ZZ \to \mu^+\mu^-\mu^+\mu^-$ candidate selected at 199.5 GeV centre-of-mass energy. Three muons are observed in the barrel and one in the forward part of the detector (the muon track going to the left is out of the plane). A kinematic fit was performed assuming the production of two identical heavy objects, each decaying into $\mu^+\mu^-$. Out of two possible combinations to form the $\mu^+\mu^-$ pairs the highest probability was found for the top-bottom and left-right pairs. The corresponding fitted invariant mass, 90.8 GeV/c^2, is fully compatible with ZZ production.

invariant and recoil masses close to the Z mass, and by large missing energy. Although it has different production kinematics, the WW process also contributes to these final states with a large cross-section. A significant fraction of the corresponding events have exactly the same features and constitute a substantial background.

9.1   Selection procedure

To ensure good reconstruction, tracks were required to have impact parameters at the interaction point smaller than 3.0 and 0.5 cm, respectively in the projections containing the beam axis and perpendicular to it, and polar angles between $20°$ and $160°$. Events with two particles identified as e^+e^- or $\mu^+\mu^-$ (using the looser identification criteria described in [12] and calorimetric requirements), were selected if their total energy was less than 60% of $\sqrt{s}$, if the angle between them was in the range $[\theta_{min}, 170°]$, where $\theta_{min} = 0.95 \arccos\left(1 - 8m_Z^2/s\right)$, if the polar angle of the event missing momentum was between $25°$ and $155°$, and if the reconstructed invariant masses satisfied:

$$\min\{\mid M_Z - m(l^+l^-) \mid, \mid M_Z - m_{recoil}(l^+l^-) \mid\} < 4 \text{ GeV/c}^2,$$
$$\max\{\mid M_Z - m(l^+l^-) \mid, \mid M_Z - m_{recoil}(l^+l^-) \mid\} < 8 \text{ GeV/c}^2,$$

where $m_{recoil}(l^+l^-)$ is the invariant mass recoiling against the l^+l^- pair. Final state radiation for candidate electrons was taken into account as discussed in Section 8.1 for the four-lepton analysis.

9.2 Results

The observed and predicted numbers of selected events are shown in Table 9. They are in overall agreement within the statistical errors. These results were used to derive the combined values of the NC02 cross-section described in Section 10.

$\sqrt{s}$ [GeV]	Integrated luminosity [pb^{-1}]	Selection efficiency	Predicted background	Predicted total MC	Selected data
	$ZZ \to \nu\bar{\nu}\mu^+\mu^-, \nu\bar{\nu}e^+e^-$				
183	54.0	0.30	0.31	0.42	0
189	158.1	0.32	0.80	1.65	2
192	25.8	0.35	0.16	0.34	2
196	76.9	0.33	0.74	1.32	2
200	84.3	0.32	0.72	1.39	1
202	41.1	0.29	0.36	0.68	0
205	83.3	0.27	0.58	1.18	1
207	141.8	0.25	1.00	1.94	2
Total	665.3	0.30	4.67	8.92	10

Table 9: Integrated luminosities, selection efficiencies and number of observed and expected selected events in the $ZZ \to \nu\bar{\nu}\mu^+\mu^-, \nu\bar{\nu}e^+e^-$ channels.

9.3 Systematic errors

The main sources of systematic error in the analysis of the $ZZ \to \nu\bar{\nu}l^+l^-$ decay modes with $l = e, \mu$ were from the statistics of the Monte Carlo samples produced to compute the remaining background and the selection efficiency and from uncertainties in the background level. These three uncertainties were propagated into the combination described in Section 10. They amounted to $\pm13\%$, $\pm5\%$ and $\pm5\%$ relative errors on the cross-sections obtained in this channel, respectively, and dominated over experimental errors in the selection efficiency and over uncertainties from approximations used to translate the results in terms of NC02 cross-sections. The third error was assumed to be fully correlated between the energies analysed.

10 Combined NC02 cross-sections

The measurements described in the previous sections for the different ZZ channels show reasonable agreement between the data and simulation. In this section the comparison is presented in terms of extracted NC02 cross-sections combined over all channels at

each centre-of-mass energy, as well as over all energies by normalising to the SM predictions, both separately in each channel, and for all channels together. Such combinations enable more comprehensive and statistically meaningful checks of the SM prediction. Cross-sections for individual sub-channels are also given at each energy in the case of the most important ZZ final states.

10.1 Likelihood method

To obtain the cross-section information in the different cases, probability functions at each energy and for each sub-channel, defined with respect to variations of the value of the NC02 cross-section, were combined into global likelihoods. For the channels $q\bar{q}q\bar{q}$ and $\nu\bar{\nu}q\bar{q}$ (analysed in the IDA stream), the shapes of the probability functions were derived from the fits to the distributions of the combined variables defined in each analysis. For the remaining channels the Poissonian probabilities were constructed, based on the numbers of events selected in the data and predicted in the simulation. The central value for each measurement was defined as the median of the corresponding likelihood. The statistical errors were obtained from the two intervals on either side of the median each containing 34.13% of the total probability. In cases when less than 31.74% of the probability was below the maximum of the likelihood, an upper limit was given, defined as the value which was exceeded by 5% of the integrated probability distribution.

10.2 Propagation of systematic errors

The propagation of systematic uncertainties affecting each different final state to its probability function was studied by introducing appropriately modified assumptions for backgrounds and efficiencies (as described in the corresponding sections). The following procedure was applied to propagate all systematic errors in the combination of any selection of channels or energy points. Uncertainties were divided into four groups according to their correlation among energies and channels. The only significant channel-correlated uncertainties were on the integrated luminosities collected at each centre-of-mass energy. They amounted to $\pm 0.3\%$ (theory error) and $\pm 0.6\%$ (measurement error) and were respectively treated as fully correlated and uncorrelated among the energies.

A set of Gaussian random numbers was then drawn and used to assign values for each kind of error taking into account its nature (common random number among channels or energies in cases of fully correlated errors, and independent ones otherwise). The probability functions were then modified accordingly and their combination was repeated a large number of times. The standard deviation of the Gaussian-like distribution of central values obtained was taken to represent the total systematic error affecting the combined measurement for the selection of channels or energy points considered.

10.3 Results and discussion

The measured values of the NC02 cross-section at each centre-of-mass energy are listed in Table 10 and shown in Figure 11, together with the SM predictions from the YFSZZ generator [32]. These measurements, normalised to the predicted SM values, were also combined into a single value:

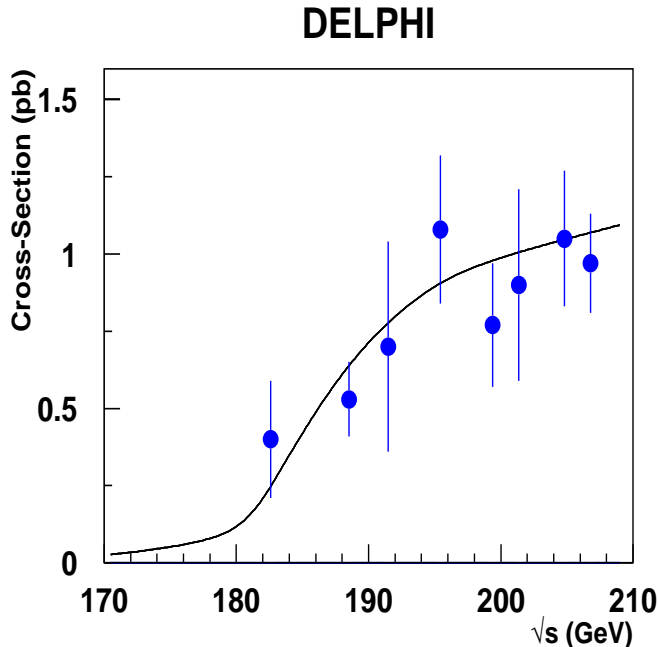$$R_{NC02} = 0.91 \pm 0.08 \ (stat) \pm 0.02 \ (syst).$$

DELPHI

Figure 11: Combined NC02 cross-sections measured from data collected in 1997-2000. The errors shown are sums in quadrature of the statistical and systematic errors. The solid curve is the SM prediction computed using the `YFSZZ` generator [32]. The corresponding uncertainty is about $\pm 2\%$ [21]. Values obtained with the `EXCALIBUR` generator were consistent with these predictions within 1%.

The systematic errors at individual energies and in the combination had the same magnitude because the main uncertainties were fully correlated. The measurements at $\sqrt{s} = 183$ and 189 GeV were compatible with those previously obtained [7]. The uncertainty in the SM prediction, of about $\pm 2\%$ [21], is not shown (as for the other results in this section). A good overall agreement with the SM prediction can be observed. The expected weights of each measurement in the combination are given in Table 10.

The combination of the results from the different energies was also performed for each channel separately. The results are listed in Table 11, with their expected weight in the global combination, and with the corresponding ZZ branching fractions predicted in the SM. The results are also shown graphically in Figure 12. The channels were ordered according to their expected weight. This order was not always correlated to the decay branching ratios because of the different background conditions. As can be seen, the three main channels $ZZ \rightarrow q\bar{q}q\bar{q}, \nu\bar{\nu}q\bar{q}$ and $l^+l^-q\bar{q}$ (with $l = e, \mu$) had similar weights, and accounted for over 90% of the total sensitivity. A good overall agreement with the SM predictions can be observed. The combination was also performed for the probabilistic $\nu\bar{\nu}q\bar{q}$ cross-check analysis, and the result obtained: $R_{NC02} = 0.80^{+0.19}_{-0.18}$ (where the errors are statistical), was consistent with that obtained from the main IDA analysis. This channel had the largest systematic uncertainty of all (relative to statistical errors). However, in this channel as in all others, systematic uncertainties were much smaller than the statistical errors. In the four-lepton channel, only an upper limit (quoted at 95% CL) is given. The χ^2 of the seven measurements had a probability of 70%.

$\sqrt{s}$ [GeV]	σ_{NC02} [pb]	SM prediction [pb]	Expected weight [%]
183	$0.40^{+0.21}_{-0.16} \pm 0.02$	0.25	1.8
189	$0.53^{+0.12}_{-0.11} \pm 0.02$	0.65	17.4
192	$0.70^{+0.37}_{-0.31} \pm 0.02$	0.78	3.6
196	$1.08^{+0.25}_{-0.22} \pm 0.02$	0.90	12.7
200	$0.77^{+0.21}_{-0.18} \pm 0.02$	0.99	15.1
202	$0.90^{+0.33}_{-0.29} \pm 0.02$	1.00	7.3
205	$1.05^{+0.23}_{-0.20} \pm 0.02$	1.05	14.8
207	$0.97^{+0.16}_{-0.15} \pm 0.02$	1.07	27.3

Table 10: Measured and predicted NC02 cross-sections at the different energy points. In the column with measured values, the first errors are statistical and the second systematic. The SM prediction was computed using the YFSZZ generator [32]. The uncertainty on these predictions is about $\pm 2\%$ [21]. Values obtained with the EXCALIBUR generator were consistent with these predictions within 1%. The last column contains the expected weight of each energy point in the global combination performed over all energies described in the text.

Channel	R_{NC02}	Expected weight [%]	Branching Fraction [%]
$q\bar{q}q\bar{q}$	$1.05^{+0.14}_{-0.14} \pm 0.04$	37.3	48.9
$\nu\bar{\nu}q\bar{q}$	$0.78^{+0.15}_{-0.15} \pm 0.05$	24.2	28.0
$\mu^+\mu^-q\bar{q}$	$0.93^{+0.22}_{-0.20} \pm 0.03$	15.6	4.6
$e^+e^-q\bar{q}$	$0.78^{+0.22}_{-0.19} \pm 0.03$	14.3	4.6
$\tau^+\tau^-q\bar{q}$	$1.12^{+0.40}_{-0.34} \pm 0.12$	5.5	4.6
$l^+l^-l^+l^-$	< 1.88	1.6	0.4
$\nu\bar{\nu}l^+l^-$	$1.52^{+0.86}_{-0.70} \pm 0.11$	1.5	2.7

Table 11: Ratios of measured to predicted cross-sections for individual channels combined over all energy points (for the two last channels $l = e, \mu$). The predicted cross-sections used are listed in Table 10. The upper limit given for the $l^+l^-l^+l^-$ channel corresponds to a 95% confidence level. In the column with measured values, the first errors are statistical and the second systematic. The two last columns contain the weight of the channel in the global combination over all channels described in the text, and the corresponding ZZ SM branching fraction.

Finally, for completeness, the values of the measured cross-sections normalised to the SM predictions are also presented at each energy in Table 12 for the three dominant channels.
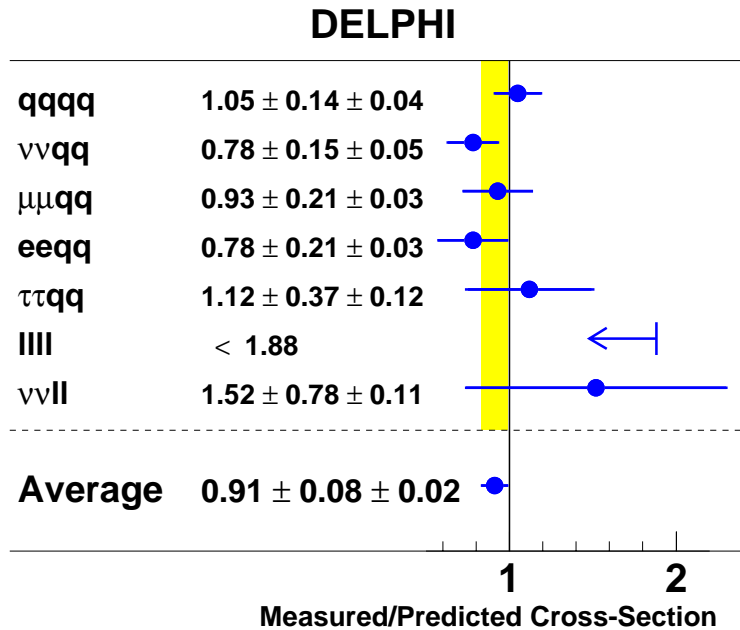

DELPHI

qqqq	$1.05 \pm 0.14 \pm 0.04$	
νν**qq**	$0.78 \pm 0.15 \pm 0.05$	
μμ**qq**	$0.93 \pm 0.21 \pm 0.03$	
eeqq	$0.78 \pm 0.21 \pm 0.03$	
ττ**qq**	$1.12 \pm 0.37 \pm 0.12$	
llll	< 1.88	
νν**ll**	$1.52 \pm 0.78 \pm 0.11$	
Average	$0.91 \pm 0.08 \pm 0.02$	

Measured/Predicted Cross-Section

Figure 12: Ratios of measured to predicted cross-sections for individual channels combined over all energy points (for the two last channels $l = e, \mu$). The predicted cross-sections used are listed in Table 10. The errors shown are sums in quadrature of the statistical and systematic errors. The vertical band displays the total error on the combination of the seven channels. The upper limit given for the $l^+l^-l^+l^-$ channel corresponds to a 95% confidence level.

Acknowledgements

$\sqrt{s}$ [GeV]	$q\bar{q}q\bar{q}$	$\nu\bar{\nu}q\bar{q}$	$l^+l^-q\bar{q}$ $(l=e,\mu)$
183	< 4.21	< 3.72	$3.49^{+2.15}_{-1.54}$
189	$1.03^{+0.39}_{-0.33}$	$0.59^{+0.34}_{-0.28}$	$0.98^{+0.41}_{-0.32}$
192	$1.34^{+0.84}_{-0.67}$	< 2.27	< 2.83
196	$1.71^{+0.52}_{-0.47}$	$1.36^{+0.54}_{-0.45}$	$0.93^{+0.51}_{-0.37}$
200	$0.78^{+0.35}_{-0.28}$	$0.63^{+0.41}_{-0.34}$	$1.10^{+0.48}_{-0.37}$
202	$1.12^{+0.55}_{-0.45}$	$1.31^{+0.82}_{-0.64}$	< 1.41
205	$1.17^{+0.37}_{-0.32}$	$0.68^{+0.42}_{-0.34}$	$0.90^{+0.42}_{-0.33}$
207	$1.02^{+0.25}_{-0.22}$	$0.91^{+0.34}_{-0.29}$	$0.78^{+0.31}_{-0.24}$

Table 12: Measured cross-sections normalised to the SM predictions for individual channels at individual centre-of-mass energies. The predicted cross-sections used are listed in Table 10. The quoted errors are statistical. The upper limits shown correspond to a 95% confidence level.

References

[1] L3 Collaboration, M. Acciarri et al., Phys. Lett. **B450** (1999) 281.

[2] D. Chang, W-Y Keung and P.B. Pal, Phys. Rev. **D51** (1995) 1326.

[3] K. Agashe, N.G. Deshpande, Phys. Lett. **B456** (1999) 60.

[4] K. Hagiwara, R.D. Peccei, D. Zeppenfeld and K. Hikasa, Nucl. Phys. **B282** (1987) 253.

[5] The LEP Collaborations ALEPH, DELPHI, L3 and OPAL, the LEP Electroweak Working Group and the SLD Heavy Flavours and Electroweak Groups, *A combination of Preliminary Electroweak Measurements and Constraints on the Standard Model*, CERN-EP/2002-091 (also hep-ex/0212036).

[6] DELPHI collaboration, P.Abreu et al., Phys. Lett. **B499** (2001) 23.
DELPHI collaboration, J.Abdallah et al., Eur. Phys. J. **C23** (2002) 409.

[7] DELPHI Collaboration, P. Abreu et al., Phys. Lett. **B497** (2001) 199.

[8] ALEPH Collaboration, R. Barate *et al.*, Phys. Lett. **B469** (1999) 287.

[9] L3 Collaboration, M. Acciarri *et al.*, Phys. Lett. **B465** (1999) 363.
L3 Collaboration, M. Acciarri *et al.*, Phys. Lett. **B497** (2001) 23.

[10] OPAL Collaboration, G. Abbiendi *et al.*, Phys. Lett. **B476** (2000) 256.

[11] DELPHI Collaboration, P.Aarnio *et al.*, Nucl. Instr. and Meth. **A303** (1991) 233.

[12] DELPHI Collaboration, P.Abreu *et al.*, Nucl. Instr. and Meth. **A378** (1996) 57.

[13] DELPHI Silicon Tracker Group, P. Chochula *et al.*, Nucl. Instr. and Meth. **A412** (1998) 304.

[14] F.A. Berends, R. Pittau, and R. Kleiss, Comp. Phys. Comm. **85** (1995) 437;
see also *Physics at LEP2* G. Altarelli, T. Sjöstrand and F. Zwirner (eds.) CERN 96-01 (1996) Vol. 2, 23.

[15] T. Sjöstrand, Comp. Phys. Comm. **82** (1994) 74;
see also *Physics at LEP2* G. Altarelli, T. Sjöstrand and F. Zwirner (eds.) CERN 96-01 (1996) Vol. 2, 41.

[16] J. Fujimoto et al., Comp. Phys. Comm. **100** (1997) 128;
see also *Physics at LEP2* G. Altarelli, T. Sjöstrand and F. Zwirner (eds.) CERN 96-01 (1996) Vol. 2, 30.

[17] S. Jadach, B.F.L. Ward, Z. Was, Comp. Phys Comm. **124** (2000) 233;
see also S. Jadach, B.F.L. Ward, Z. Was, Comp. Phys Comm. **79** (1994) 503.

[18] S. Jadach, W. Placzek, B.F.L. Ward, Phys. Lett **B390** (1997) 298.

[19] T. Alderweireld *et al.*, CERN-OPEN-2000-141.

[20] F. A. Berends, P. H. Daverveldt, R. Kleiss, Comp. Phys. Comm. **40** (1986) 271-284, 285-307, 309.

[21] E. Accomando *et al.*, *Four-fermion production in electron-positron collisions*, Reports of the working groups on precision calculations for LEP2 Physics, S. Jadach, G. Passarino, R. Pittau (eds.) CERN 2000-009 (2000), 1.

[22] P. Abreu *et al.*, Nucl. Instr. and Meth. **A427** (1999) 487.

[23] S. Catani *et al.*, Phys. Lett **B269** (1991) 432.
N. Brown and W.J. Stirling, Z. Phys. **C53** (1992) 629.

[24] DELPHI Collaboration, P. Abreu *et al.*, Phys. Lett **B462** (1999) 410.

[25] See section 5.2 in DELPHI Collaboration, P. Abreu *et al.*, Eur. Phys. J. **C2** (1998) 581.

[26] DELPHI Collaboration, J. Abdallah *et al.*, CERN EP 2002-088 (2002);
G.Borisov, Nucl. Instr. Meth. **A417** (1998) 384.

[27] A. Ballestrero *et al.*, *Report of the QCD Working Group*, Reports of the working groups on precision calculations for LEP2 Physics, S. Jadach, G. Passarino, R. Pittau (eds.) CERN 2000-009 (2000), 137.

[28] DELPHI Collaboration, P. Abreu *et al.*, Z. Phys. **C73** (1996) 11.

[29] DELPHI Collaboration, P. Abreu *et al.*, Eur. Phys. J. **C10** (1999) 415.

[30] T.G.M. Malmgren, Comp. Phys. Comm. **106** (1997) 230;
T.G.M. Malmgren and K.E. Johansson, Nucl. Instr. Meth. **A403** (1998) 481.

[31] T. Sjöstrand, Comp. Phys. Comm. **28** (1983) 229.

[32] S. Jadach, W. Placzek, B.F.L. Ward, Phys. Rev. **D56** (1997) 6939.